Computational and Experimental Investigations of the Flow Around Cavitating Hydrofoils

by

Neal E. Fine

B.S., University of Rochester (1986)

Submitted in Partial Fulfillment of the Requirements
for the Degree of Master of Science in Ocean Engineering

at the

Massachusetts Institute of Technology

August, 1988

Signature of Author _____

Department of Ocean Engineering

August, 1988

Certified by _____

Professor J.E. Kerwin

Thesis Supervisor

Accepted by _____

Professor A. Douglas Carmichael

Chairman, Department Graduate Committee

Computational and Experimental Investigations of the Flow Around Cavitating Hydrofoils

Neal E. Fine

Department of Ocean Engineering

Abstract

The linearized boundary value problem of the two dimensional cavitating hydrofoil of general shape has been solved semi-analytically by inversion of the singular integral equations describing the unknown source and vortex distributions and the subsequent numerical integration over such known functions as the slope of the wetted foil surface. However, a more desirable method of solution is one which permits a natural extension to the solution of three dimensional wing and propeller cavitation. The method of discrete singularities, which has the advantage of being the two dimensional analog of the vortex lattice method, has been studied extensively for this reason. The current research included the extension of the method to solve the the most general problems of partial and supercavitation with the correct points of cavity detachment and the most physically acceptable closure model. The results of an experiment in the MHL water tunnel show good agreement with numerical results. The correlation between numerical and experimental cavitation numbers, along with the latest extensions to the analysis, is presented.

Aknowledgements

I would like to acknowledge the continuous and invaluable aid and advice provided by Dr. Spyros Kinnas during all phases of this research. In particular, his contributions to the analysis of face cavitation and midchord detachment were significant.

The support, technical and otherwise, of Professor J.E. Kerwin and the rest of the propeller group is gratefully acknowledged.

Finally, in the preparation of this document, the tedious job of proofing went to the dynamic tandem of Kelly Morris and Andrea Novacky. Without their intelligent suggestions, I would be much less satisfied.

This research was sponsored in part by the Naval Sea Systems Command General Hydromechanics Research Program administered by the David W. Taylor Naval Ship Research and Development center, and in part by the Volvo Penta Corporation.

Contents

List of Figures

Chapter 1

Introduction

Cavitation is the formation of regions of vapor in a liquid near points of minimum pressure. For almost a century it has been known as a cause of efficiency decrement and structural failure in propulsors and turbomachinery. To Naval Architects and Marine Engineers, cavitation is particularly notorious as a principal contributor to flow noise emanating from cavitating propellers. Perhaps a more surprising effect, however, is the intense material corrosion due to the high impulse forces which exist at points where the unsteady cavities collapse. In fact, it is this unsteady nature of cavitation which induces vibrations, often causing expensive hull and machinery fatigue and subsequent failure. These are the salient effects of cavitation and they are overwhelmingly detrimental. Therefore, there is ample motivation for understanding cavitation with the goal of controlling it or designing around it. For example, the lift and drag characteristics of cavitating marine hydrofoils are often required for the purpose of efficiency control. This gives rise to an analysis problem similar to the analysis problem of non-cavitating hydrofoils.

This thesis describes developments in the linearized solution to the analysis problem of the flow around cavitating hydrofoils, as well as pertinent experimental results.

1.1 Objectives

There were four main objectives in the current research:

(1) The first goal was to continue the investigation and development of a numerical method for solving the linearized partially cavitating hydrofoil problem in two dimensions and to ap-

ply this numerical method to the case of a *supercavitating* hydrofoil. Ultimately, the purpose of studying the numerical method in two dimensions is to apply new knowledge to the numerical solution of three dimensional propeller cavitation. For example, a comprehensive study of the effect of non-linear corrections to a numerical solution of the linearized two dimensional partial cavitation problem was completed by Corrado (1986). His research led to the implementation of the non-linear corrections to the propeller analysis program, PUF-3 (for a complete description, see [8]). As a continuation of this, the current research includes an investigation of the effect of an open cavity model on the same numerical solution with the goal of implementing the model in PUF-3. The open cavity model allows for a small wake thickness trailing the partial cavity.

(2) The second objective was to modify existing codes which solve the problems of partial and supercavitation analytically. The original codes, written by Kinnas in the course of his PhD research, were modified to solve the problems of partial and supercavitation for *general* hydrofoil geometry and were then linked to the numerical code to provide easy comparison. This coupling of the numerical and analytical solutions was especially useful in evaluating the accuracy of the numerical method.

(3) The third goal was to obtain experimental measurements of the cavitation number, σ, for a partially cavitating hydrofoil with various cavity lengths. Comparison of the experimental and numerical results, after including in the model the tunnel wall effect and the effect of the boundary layer, as well as a measured value for the openness of the cavity at its trailing edge, allows for a general appraisal of the accuracy of the numerical model. The thickness of the cavity wake was measured by comparing the displacement thicknesses of the hydrofoil with and without cavitation. This result is particularly important since the cavity wake thickness is not obtained from analysis.

(4) The final goal was to modify the analytic and numerical solutions to handle detachment of the supercavity aft of the leading edge on the suction side of the foil and forward of the trailing edge on the pressure side of the foil. In this way, the existing analysis tools have been generalized to handle the four observed forms of supercavitation.

1.2 Definitions

Cavitation is defined as the formation of a region of vapor in a flow field near a local pressure minimum. Although the inception of cavitation is affected by many parameters (i. e. , viscosity, dissolved gas content, ambient pressure and turbulence intensity, etc.) it is reasonable to assume that a cavity forms at or near the saturation vapor pressure and that the resulting cavity volume consists solely of fluid in the vapor phase. It should be noted, however, that this neglects the results of a substantial amount of research (1950's to present) investigating cavitation inception. In summary, experimental investigations have shown that:

1. cavity inception does not necessarily occur when the fluid pressure falls below the vapor pressure, but is largely dependent on the existence of gas or vapor *nuclei*.

2. cavity inception is a dynamically complicated phenomenon which is not likely to be included in an engineering analysis tool such as the one being developed here.

The cavitation number

$$\sigma \equiv \frac{P_\infty - P_v}{\frac{1}{2}\rho U_\infty^2} \tag{1.1}$$

measures the *likelihood* of cavitation. That is, if U_∞ and P_∞ are the steady velocity and pressure far upstream from a body in uniform flow, and P_v is the saturation vapor pressure in an incompressible fluid of density ρ, then the lower the cavitation number the more likely it is that the body will cavitate. There is a one-to-one correlation between cavitation number and cavity length, with the zero cavitation number limit corresponding to an infinitely long cavity.

It is assumed that cavity inception occurs when the fluid pressure is equal to or less than the vapor pressure. Another form of this requirement comes from the steady Bernoulli equation and the definition of the cavitation number. Namely, cavitation occurs when

$$\sigma \leq -C_{p_{min}} \tag{1.2}$$

where C_p is the nondimensional pressure

$$C_p \equiv \frac{P - P_\infty}{\frac{1}{2}\rho U_\infty^2}. \tag{1.3}$$

For the specific case of the marine propeller, cavitation commonly occurs near the leading edge of an individual blade where local high velocities (and therefore low pressures) result from the large blade slopes. Clearly, in an incompressible, inviscid, irrotational fluid, in which the velocity field is the gradient of a scalar potential, the minimum pressure exists on the surface of the blade. Moreover, it can be shown that for a body with a laminar boundary layer prior to cavitation, the normal pressure gradient is such that the pressure increases away from the body. Thus, a cavity which grows at a point where the fluid pressure falls below the vapor pressure does so on the surface of the blade and stays there.

The two dimensional propeller analog is a cambered hydrofoil with thickness and oriented at an angle with respect to a uniform inflow. The goal is to determine the cavity shape, lift, and drag for a specific hydrofoil shape and cavitation number. However, the two dimensional problem is actually solved by assuming a cavity *length* and solving for the cavitation number. The problems of *partial cavitation* (cavity length less than the chord length), shown in Figure 1.1, and *supercavitation* (cavity length greater than the chord length), shown in Figure 1.2, will be considered separately since the boundary conditions are different. Chapter 2 describes the set-up and solution of the two boundary value problems, with emphasis on the numerical solution via the method of discrete singularities. Chapter 3 presents the results of an experiment with partial cavitation, providing complete comparison of experimental and numerical results. Finally, Chapter 4 presents the analytic solution to the problem of cavity detachment aft of the leading edge on the suction side of a supercavitating hydrofoil.

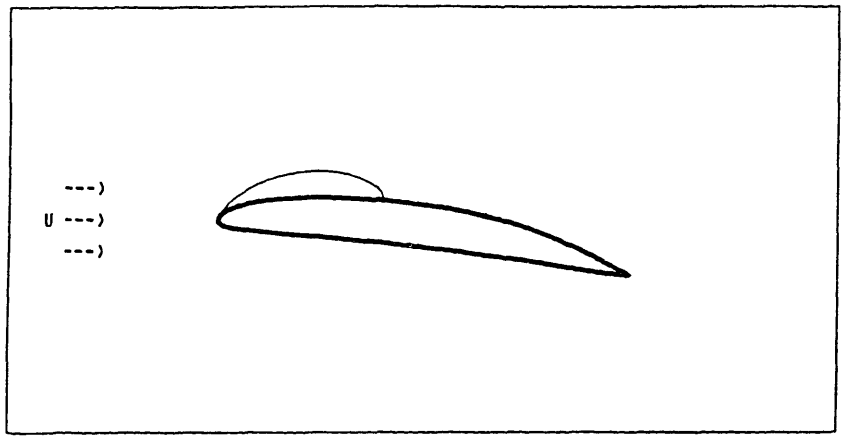

Figure 1.1: Partially cavitating hydrofoil

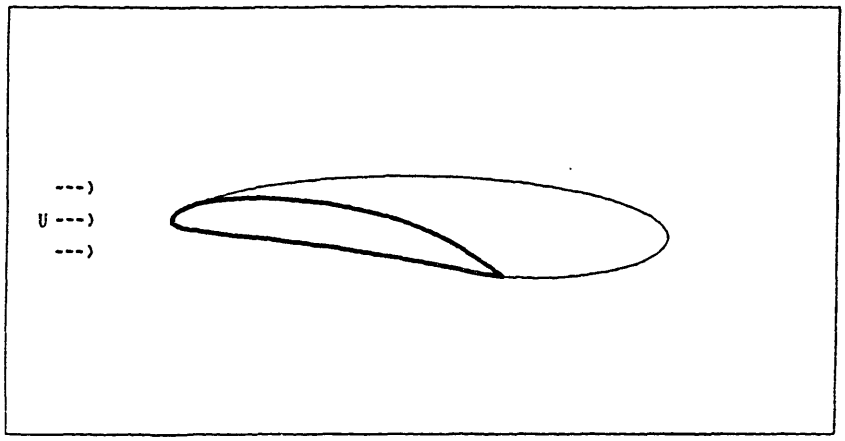

Figure 1.2: Supercavitating hydrofoil

Chapter 2

Analytical and Numerical Considerations

The analysis of flow around cavitating bluff bodies has been achieved by methods of conformal mapping for simple geometries and for the zero cavitation number limit [2]. However, for non-zero cavitation numbers a cavity termination model must be invented to account for the stagnation point after and near the cavity's trailing edge while maintaining constant total velocity on the cavity boundary (free streamline theory). Two of the most prominent termination models are the Riabouchinsky model and the re-entrant jet model. No consensus as to which is correct has yet been reached [19]. Aside from this dilemma, and despite the obvious attraction to an exact non-linear solution, the method of conformal mapping is still cumbersome for solving the problem with general hydrofoil geometry. For this reason, we turn to the solution of the *linearized* boundary value problem, for which there is no need to choose an arbitrary cavity termination model.

2.1 Linear Theory for Cavitating Hydrofoils

2.1.1 Partial Cavitation

Consider a stationary partially cavitating hydrofoil whose foil thickness $\tau(x)$, cavity thickness $h(x)$, and foil camber $\eta(x)$ are all small in comparison to the chord length (see Figure 2.1). The fluid is ideal and irrotational. The inflow is uniform and steady, the field is infinite, and the velocity potential satisfies Laplace's equation

$$\nabla^2 \Phi = 0 \tag{2.1}$$

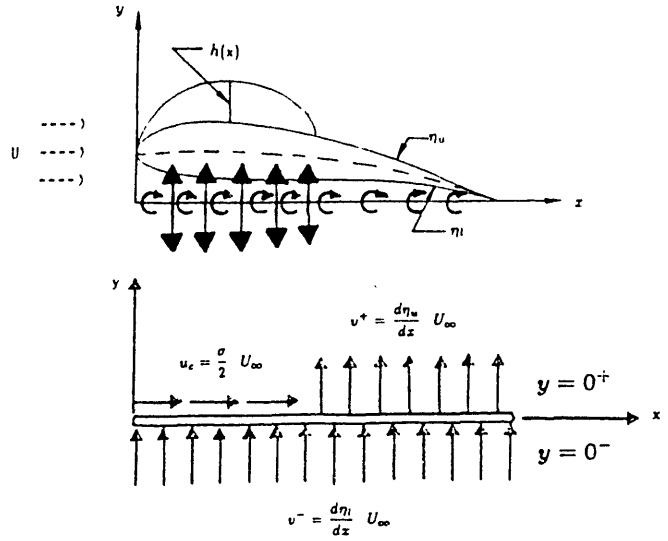

Figure 2.1: Linearized boundary conditions for partial cavitation.

where

$$\Phi = \phi + U_\infty x.$$

Here U_∞ is the fluid velocity at infinity, oriented parallel to the x-axis, and ϕ is the perturbation velocity potential, which also satisfies Laplace's equation. Thus,

$$\begin{aligned} \frac{\partial \Phi}{\partial x} &= u + U_\infty \\ \frac{\partial \Phi}{\partial y} &= v \end{aligned} \tag{2.2}$$

$$\begin{aligned} \nabla \Phi &\rightarrow (U_\infty, 0) \quad at\ \infty \\ or: \quad \phi &\rightarrow 0 \quad at\ \infty \end{aligned} \tag{2.3}$$

The linearized boundary value problem for partial cavitation with cavity detachment at the leading edge of the hydrofoil is stated by Laplace's equation (2.1) and the following boundary conditions:

$$v_u(x) = U_\infty \frac{d}{dx}\left(\eta(x) + \frac{\tau(x)}{2}\right) = U_\infty \frac{d\eta_u}{dx} \qquad l < x < 1 \quad on\ y = 0^+ \tag{2.4}$$

$$v_l(x) = U_\infty \frac{d}{dx}\left(\eta(x) - \frac{\tau(x)}{2}\right) = U_\infty \frac{d\eta_l}{dx} \qquad 0 < x < 1 \quad on\ y = 0^- \tag{2.5}$$

where v_u is the vertical velocity on the upper side of the foil, v_l is the vertical velocity on the lower side of the foil, and l is the length of the cavity normalized on the chord length. The

kinematic boundary conditions (2.4) and (2.5) are due to the linearization of the slope of the total velocity at the foil surface which must match the slope of the foil surface.

A dynamic boundary condition results from an application of the steady Bernoulli equation at the cavity boundary, where the cavity pressure is equal to the vapor pressure

$$P_c = P_v.$$

Thus, if q is the total velocity on the cavity surface, we have

$$P_\infty + \frac{1}{2}\rho U_\infty^2 = P_v + \frac{1}{2}\rho q^2 \tag{2.6}$$

$$\frac{P_\infty - P_v}{\frac{1}{2}\rho U_\infty^2} = \frac{q^2}{U_\infty^2} - 1. \tag{2.7}$$

Recalling the definition of the cavitation number (1.1) this simplifies to

$$q = U_\infty\sqrt{1+\sigma}. \tag{2.8}$$

The total velocity q is therefore constant along the cavity surface. This is a result of the assumption that the cavity surface is a streamline in steady flow and that the cavity pressure is constant along the streamline. Note that this is a fully non-linear result.

The linearized dynamic boundary condition, derived first by Tulin [18], is obtained by expanding (2.8) in terms of u and v and retaining only the first order perturbation terms, leaving

$$u = \frac{\sigma}{2}U_\infty \qquad 0 < x < l \quad on\ y = 0^+. \tag{2.9}$$

Equations (2.1), (2.4), (2.5), and (2.9) define the linearized boundary value problem for the partially cavitating hydrofoil in two dimensions.

Solutions to (2.1) which satisfy the condition that $\phi \to 0$ at ∞ include sources and vortices arrayed on the horizontal projected axis of the hydrofoil (see Figure 2.1). Since the source and vortex potentials each satisfy the partial differential equation (2.1), *distributions* of the singularities may be superposed to form a general solution.

The kinematic boundary conditions (2.4) and (2.5) along with the dynamic boundary condition (2.9) specify the vertical and horizontal perturbation velocities on the surface of the

foil and cavity. The velocities induced by the singularities on the foil and cavity boundaries must match those prescribed by these boundary conditions. This requirement, as derived by Kinnas [9], yields the following integral equations for the unknown source and vortex strengths:

$$v_u(x) = \frac{q_\tau(x)}{2} + \frac{1}{2\pi}\int_0^1 \frac{\gamma(\xi)d\xi}{\xi - x} = U_\infty \frac{d\eta_u}{dx} \quad on\ y = 0^+ \qquad l < x < 1 \tag{2.10}$$

$$v_l(x) = -\frac{q_\tau(x)}{2} - \frac{q_c(x)}{2} + \frac{1}{2\pi}\int_0^1 \frac{\gamma(\xi)d\xi}{\xi - x} = U_\infty \frac{d\eta_l}{dx} \quad on\ y = 0^- \qquad 0 < x < 1 \tag{2.11}$$

$$u_c(x) = \frac{\gamma(x)}{2} - \frac{1}{2\pi}\int_0^1 \frac{q_\tau(\xi)d\xi}{\xi - x} - \frac{1}{2\pi}\int_0^l \frac{q_c(\xi)d\xi}{\xi - x} = U_\infty \frac{\sigma}{2} \quad on\ y = 0^+ \qquad 0 < x < l \tag{2.12}$$

where $u_c(x)$ is the horizontal perturbation velocity on the cavity surface.

The cavity source distribution is related to the local slope of the cavity surface $h(x)$

$$q_c(x) = U_\infty \frac{dh}{dx}.$$

Similarly, the foil thickness source strength $q_\tau(x)$ is related to the local slope of the fully wetted foil

$$q_\tau(x) = U_\infty \frac{d\tau}{dx}. \tag{2.13}$$

The partially cavitating hydrofoil problem may be decomposed into camber, thickness, and angle of attack problems as shown in Figure 2.2. This decomposition, when applied to equations (2.10) and (2.11), yields a single kinematic boundary condition. The boundary value problem is completed by imposing the Kutta condition and the cavity closure condition. The Kutta condition requires that there be no flow around the trailing edge which, in linear theory, is equivalent to the requirement that there be no vorticity at the trailing edge. The cavity closure condition requires that the cavity sources sum to zero, which is equivalent to the requirement $h(l) = 0$.

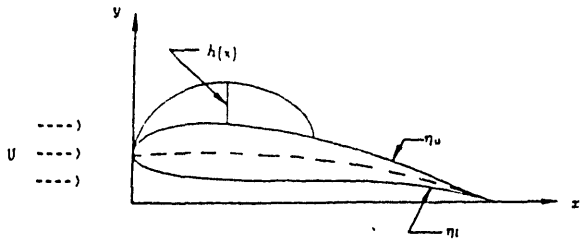

$$\eta_u(x) = \eta(x) + \frac{h(x)}{2} + \frac{\tau(x)}{2} + \frac{h(x)}{2}$$

$$\eta_l(x) = \eta(x) + \frac{h(x)}{2} - \frac{\tau(x)}{2} - \frac{h(x)}{2}$$

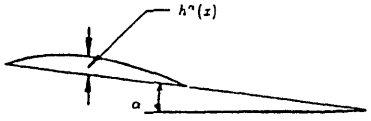

Camber $\eta(x) + \frac{h(x)}{2}$

$\updownarrow$

vorticity distribution $\gamma(x)$ $\quad 0 < x < 1$

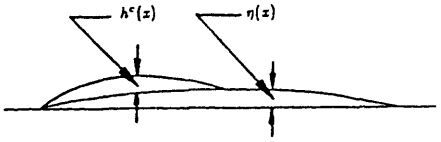

Thickness $\tau(x)$

$\updownarrow$

source distribution $\quad q_\tau(x) = U_\infty \cdot \frac{d\tau}{dx}$ $\quad 0 < x < 1$

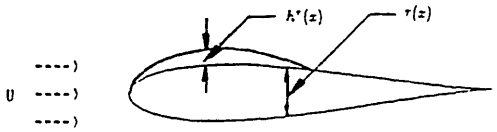

Cavity thickness h(x)

$\updownarrow$

cavity source distribution $\quad q_c(x) = U_\infty \cdot \frac{dh}{dx}$ $\quad 0 < x < l$

Figure 2.2: Linear decomposition in partial cavitation.

Finally, the linearized boundary value problem for a two dimensional partially cavitating hydrofoil includes:

1. *Kinematic Boundary Condition*

$$-\frac{q_c(x)}{2} + \frac{1}{2\pi}\int_0^1 \frac{\gamma(\xi)d\xi}{\xi - x} = U_\infty \frac{d\eta}{dx} \qquad 0 < x < 1 \qquad (2.14)$$

$$(q_c(x) = 0 \quad for \quad l < x < 1)$$

2. *Dynamic Boundary Condition*

$$\frac{\gamma(x)}{2} - \frac{1}{2\pi}\int_0^l \frac{q_c(\xi)d\xi}{\xi - x} = U_\infty \frac{\sigma}{2} + \frac{U_\infty}{2\pi}\int_0^1 \frac{\frac{d\tau}{d\xi}d\xi}{\xi - x} \qquad 0 < x < l \qquad (2.15)$$

3. *Kutta Condition*

$$\gamma(1) = 0 \qquad (2.16)$$

4. *Cavity Closure Condition*

$$\int_0^l q_c(x)dx = 0 \qquad (2.17)$$

2.1.2 Supercavitation

The decomposition for the supercavitating hydrofoil is shown in Figure 2.3[1]. The thickness problem combines the cavity thickness and the foil thickness and therefore the unknown source strength, q(x), will represent both the foil and the cavity. This is in contrast to the formulation of the partial cavitation problem in which the foil thickness and cavity thickness are considered separately. The boundary conditions are:

$$u_c = U_\infty \frac{\sigma}{2} \qquad 0 < x < l \quad on\ y = 0^+ \tag{2.18}$$

$$u_c = U_\infty \frac{\sigma}{2} \qquad 1 < x < l \quad on\ y = 0^- \tag{2.19}$$

$$v_l = U_\infty \frac{d\eta_l}{dx} \qquad 0 < x < 1 \quad on\ y = 0^-. \tag{2.20}$$

Replacing the foil and cavity by a continuous distribution of sources and vortices (Figure 2.4) and equating the induced velocities to these boundary conditions yields the following singular integral equations [10]:

1. *Kinematic Boundary Condition*

$$-\frac{q(x)}{2} + \frac{1}{2\pi}\int_0^1 \frac{\gamma(\xi)d\xi}{\xi - x} = U_\infty \frac{d\eta_l}{dx} \qquad 0 < x < 1 \tag{2.21}$$

2. *Dynamic Boundary Condition*

$$\frac{\gamma(x)}{2} - \frac{1}{2\pi}\int_0^l \frac{q(\xi)d\xi}{\xi - x} - U_\infty \frac{\sigma}{2} = 0 \qquad 0 < x < l. \tag{2.22}$$

The cavity camber in the wake of the hydrofoil, c(x), is obtained by equating the camber slope to the vertical velocity induced by the vortices on the foil and numerically integrating:

$$U_\infty \frac{dc}{dx} = v_{in}(x) = -\frac{1}{2\pi}\int_0^1 \frac{\gamma(\xi)d\xi}{\xi - x} \qquad 1 < x < l. \tag{2.23}$$

[1] Courtesy of Dr. S.A. Kinnas, Dept. of Ocean Engineering, MIT

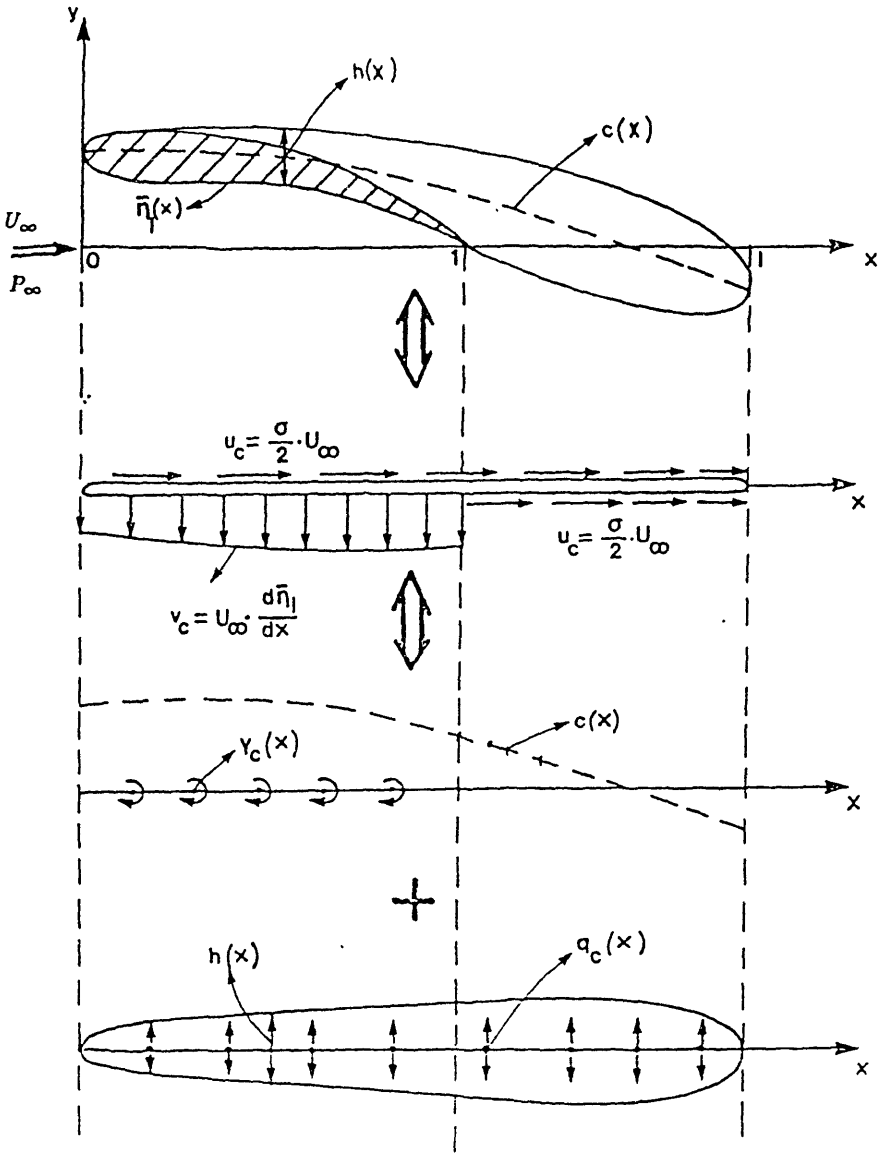

Figure 2.3: Linear decomposition in supercavitation

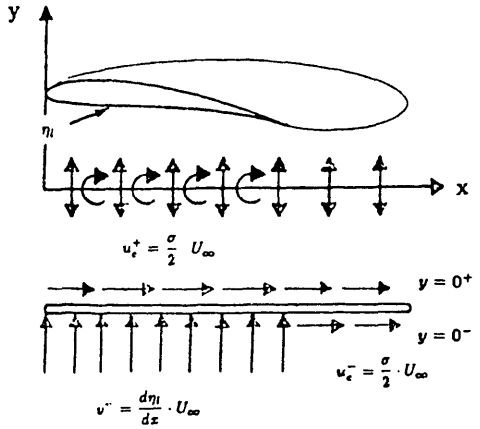

Figure 2.4: Linearized boundary conditions for supercavitation.

The boundary conditions (2.21) and (2.22), along with the Kutta condition (2.16) and the cavity closure condition (2.17), define completely the boundary value problem for the supercavitating hydrofoil.

2.2 Analytic Solution

Analytic solution to the linearized partial and supercavitation boundary value problems has been achieved by inverting the representative singular integral equations and reducing the final solution for the cavitation number and for the source and vortex distributions to integrals of known functions [11]. The known functions include the slope of the lower wetted foil surface (for supercavitation) and the horizontal perturbation velocity on the suction side of the foil under non-cavitating conditions (for partial cavitation). The payoff is that these integrals may be reduced to quadrature and the complete linear solution then depends only on the hydrofoil geometry and the length of the cavity. We call this a "semi-analytical" solution because of the numerical integrations involved. Details of the derivations may be found in Kinnas' PhD thesis.

Despite the extremely successful nature of the semi-analytical method, it is limited in application to two dimensional flows due to the complex nature of three dimensional integral equations [8]. A more desirable solution would lead naturally to the vortex lattice method which is used to solve the propeller analysis problem in three dimensions. A method which

satisfies this requirement relies on the numerical approximation of the boundary integral equations described in sections 2.1.1 and 2.1.2 and is called the *method of discrete singularities.*

2.3 Numerical Solution

2.3.1 Method of Discrete Singularities

The method of discrete singularities was developed at MIT by Golden [6], Van Houten [21], and others [13,20]. Most recently, Corrado applied the method to the problem of partially cavitating hydrofoils of selected thickness and camber forms with the goal of implementing the necessary modifications for the accurate prediction of singularity distributions and cavity shape. Results of his research included the selection of the half-cosine discretization (described below) and the implementation of the non-linear corrections described by Kinnas [11]. In the present research, the work of Corrado has been extended to solve the problem of supercavitating hydrofoils of general shape.

The discrete singularities approach consists of modeling the foil and cavity by a finite distribution of point sources and point vortices arrayed along the horizontal projected axis and whose strengths are determined by applying the *discretized* kinematic and dynamic boundary conditions at selected *control points.* The process, which is applicable to partial *and* supercavitation, is as follows:

1. Discretize the linearized foil into N panels and the linearized cavity into M panels.
2. Approximate the continuous source and vorticity distributions with discrete vortices and sources.
3. Express the singular integrals as finite sums of M unknown cavity sources Q_i, N unknown vortices Γ_i, and the known thickness sources.
4. Apply the boundary conditions at appropriate control points and solve the resulting system of N+M+1 equations for the unknown $Q_i's$, $\Gamma_i's$, and σ.

Thus, the remaining question is: where should the discrete singularities be (a) with respect to one another and (b) with respect to the control points? One possibility is the constant

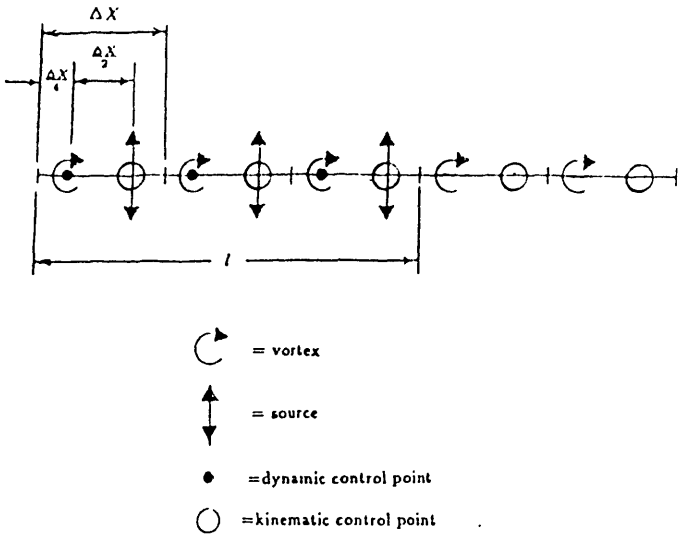

Figure 2.5: Constant spacing discretization for supercavitation.

spacing configuration (Figure 2.5), which is formed by dividing the linearized foil into N panels of equal length and modeling the foil with N point vortices spaced at the $\frac{1}{4}$ fraction of each vortex panel. The cavity is then represented by M point sources spaced at the $\frac{3}{4}$ fraction of each source panel. The kinematic control points (the points at which the kinematic boundary condition is satisfied) are superimposed on the point sources. The dynamic control points (the points at which the dynamic boundary condition is satisfied) are superimposed on the point vortices.

The strengths of the discrete point sources and point vortices are defined as

$$Q_i = \bar{q}(X_{s_i})(X_{p_{i+1}} - X_{p_i}) \tag{2.24}$$

$$\Gamma_i = \gamma(X_{v_i})(X_{p_{i+1}} - X_{p_i}) \tag{2.25}$$

assuming for now that the source and vortex panels coincide, as they do for constant spacing. The source strength is based on the average $\bar{q}_i$ rather than the local value $q(X_{s_i})$. It has been found that this is necessary to obtain the correct cavity thickness distribution [3].

The discretized boundary conditions for the cases of partial and supercavitation may be written as follows:

1. *Partial Cavitation:*

   (a) *Kinematic Boundary Condition*

$$\frac{d\eta_l}{dx} = \frac{Q_j}{2(X^s_{p_{j+1}} - X^s_{p_j})} - \frac{1}{2\pi}\sum_{i=1}^{N}\frac{\Gamma_i}{X_{k_j} - X_{v_i}} \quad j = 1, ..., N \tag{2.26}$$

   (b) *Dynamic Boundary Condition*

$$\frac{\sigma}{2} + \frac{1}{2\pi}\sum_{i=1}^{KT}\frac{\frac{dr}{d\xi}}{\xi - x} = \frac{\Gamma_j}{2(X^v_{p_{j+1}} - X^v_{p_j})} + \frac{1}{2\pi}\sum_{i=1}^{M}\frac{Q_i}{X_{d_j} - X_{s_i}} \quad j = 1, ..., M-1 \tag{2.27}$$

2. *Supercavitation:*

   (a) *Kinematic Boundary Condition*

$$\frac{d\eta_l}{dx} = -\frac{Q_j}{2(X^s_{p_{j+1}} - X^s_{p_j})} - \frac{1}{2\pi}\sum_{i=1}^{N}\frac{\Gamma_i}{X_{k_j} - X_{v_i}} \quad j = 1, ..., N \tag{2.28}$$

   (b) *Dynamic Boundary Condition*

$$0 = \frac{\Gamma_j}{2(X^v_{p_{j+1}} - X^v_{p_j})} - \frac{1}{2\pi}\sum_{i=1}^{M}\frac{Q_i}{X_{d_j} - X_{s_i}} - \frac{\sigma}{2} \quad j = 1, ..., M-1 \tag{2.29}$$

$$\begin{aligned}
N &= \textit{number of point vortices} \\
M &= \textit{number of point sources} \\
KT &= \textit{number of thickness sources} \\
\Gamma_i &= \textit{strength of the } i^{th} \textit{ vortex} \\
Q_i &= \textit{strength of the } i^{th} \textit{source} \\
X^s_{p_i} &= \textit{position of the } i^{th} \textit{ source panel boundary} \\
X^v_{p_i} &= \textit{position of the } i^{th} \textit{ vortex panel boundary} \\
X_{s_i} &= \textit{position of the } i^{th} \textit{ source} \\
X_{v_i} &= \textit{position of the } i^{th} \textit{ vortex} \\
X_{k_i} &= \textit{position of the } i^{th} \textit{ kinematic control point} \\
X_{d_i} &= \textit{position of the } i^{th} \textit{ dynamic control point}
\end{aligned} \tag{2.30}$$

The cavity closure condition may also be discretized:

$$\sum_{j=1}^{M} Q_j = 0. \tag{2.31}$$

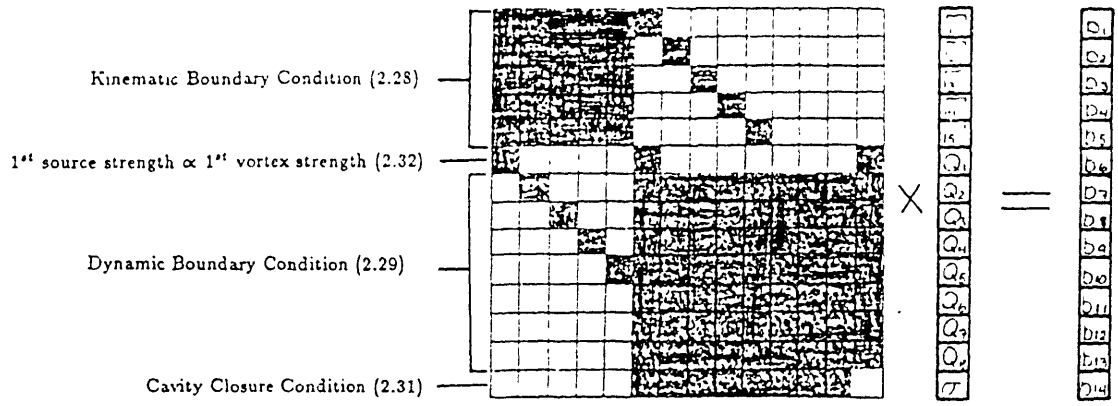

Figure 2.6: Matrix equation for supercavitation.

It has been shown [8] that the source and vortex distributions share the same fourth-root singularities near the leading edge. The strengths of the first discrete singularities are therefore proportional and related in the following way:

$$\frac{\Gamma_1}{Q_1} = \frac{\frac{3}{4} X^v_{p_1}}{(X^s_{p_1})^{\frac{3}{4}} (X_{s_1})^{\frac{1}{4}}}. \tag{2.32}$$

Since the dynamic boundary condition is not applied in the first panel, (2.32) is the final equation needed to balance the number of unknowns.

Due to the spacing of discrete singularities, the Kutta condition (2.15) is automatically satisfied [7]. Note that the upstream velocity has been normalized to unity.

Thus the problem is reduced to a system of N+M+1 algebraic equations including N kinematic boundary conditions (2.26, 2.28), M-1 dynamic boundary conditions (2.27, 2.29), the cavity closure condition (2.31), and the relation between Γ_1 and Q_1 (2.32). The unknowns include N discrete vortex strengths, M cavity source strengths, and the cavitation number. In each case, the resulting matrix equation is solved by Gaussian elimination. The form of the equation is shown in Figure 2.6 for supercavitation.

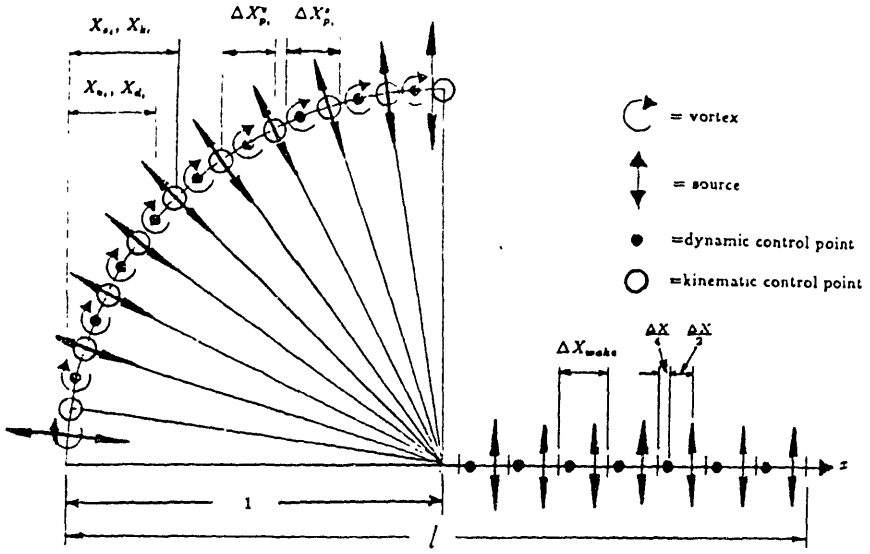

Figure 2.7: Half-cosine spacing for supercavitation.

2.3.2 Half-Cosine Spacing

Unfortunately, the results of the constant spacing technique show poor convergence to the analytic results as the number of panels is increased. For this reason, much work has been done to seek an appropriate spacing configuration with more accurate results and "quick" convergence (see Golden [6] and Corrado [3]). As a result of a comprehensive study of discretization techniques [3], it has been found that *half-cosine* spacing with singularities placed at $\frac{1}{4}$ and $\frac{3}{4}$ fractions of the angular panel (see Figure 2.7) results in more accurate singularity distributions. This is due to the appropriate representation of the leading edge singularity in source and vortex distributions [12].

The transformed angular coordinate θ is related to the chordwise coordinate x in the following way:

$$x = 1 - cos\theta \qquad 0 < \theta < \frac{\pi}{2}. \tag{2.33}$$

The linearized foil is split into N panels of varying length — small at the leading edge and growing towards the trailing edge — thus concentrating singularities at the leading edge and

resulting in more accurate representation of the singularity in vortex and source distributions.

The N point vortices are located at the points

$$X_{v_i} = 1 - cos\left(\frac{2i-1}{2}\frac{\pi}{2N}\right) \qquad i = 1, ..., N \tag{2.34}$$

and the M point sources are located at the points

$$X_{s_i} = 1 - cos\left(i\frac{\pi}{2N}\right) \qquad i = 2, ..., M \tag{2.35}$$

with the exception of the first source, which is placed at the same location as the first vortex.

The position of the kinematic and dynamic control points are determined by the zeroes of the flat plate error functions for partial cavitation

$$\Delta V(x) = -\frac{1}{2\pi}\sum_{i=1}^{N}\frac{\Gamma_i}{X_{v_i} - x} + \frac{q(x)}{2} - U_\infty \alpha \tag{2.36}$$

and

$$\Delta U(x) = -\frac{1}{2\pi}\sum_{i=1}^{M}\frac{Q_i}{X_{s_i} - x} + \frac{\gamma(x)}{2} - \frac{\sigma}{2}U_\infty. \tag{2.37}$$

Plots of these functions may be found in the paper by Kerwin and Kinnas [8]; they show that the correct kinematic and dynamic control points lie halfway between the positions of the sources and vortices, respectively (in the θ coordinate). That is, the kinematic control points coincide with the sources and the dynamic control points coincide with the vortices. It is assumed that this result will not change for supercavitation.

The source and vortex panels do not coincide as they do for constant spacing. For accurate representation of the singularity in source and vortex distributions at the trailing edge of the cavity, the cavity must end between a vortex and a source. Since the vortex panels begin and end at the source locations, and since the cavity must consist of an integral number of source panels, the source and vortex panels cannot coincide. Equations (2.24) and (2.25) must therefore be modified accordingly.

The vortex panel boundaries are located at the points

$$X^v_{p_i} = 1 - cos\left(i\frac{\pi}{2N}\right); \qquad i = 1, ..., N \tag{2.38}$$

and the source panel boundaries are located at the points

$$X^s_{p_i} = 1 - cos\left(\frac{4i+1}{4}\frac{\pi}{2N}\right); \qquad i = 2, ..., M \tag{2.39}$$

with the exception of the first source panel boundary which is located at

$$X^s_{p_1} = 1 - cos\left(\frac{3\pi}{8N}\right).$$

This source panel configuration was chosen following experimentation by Corrado [3].

Given the cavity length and the number of vortex panels, the number of sources can be determined:

1. *Partial Cavitation*

$$M = Int\left(\frac{2N}{\pi}cos^{-1}(1-l) + .25\right)$$

2. *Supercavitation*

$$M = Int\left(\frac{l-1}{sin\left(\frac{\pi}{2N}\right)} + N\right)$$

where *Int* denotes integer part. The actual cavity length therefore is always less than or equal to the input length l.

For supercavitation, the discretization on the foil is identical to that of partial cavitation, with the single aberration that the last cavity source prior to the trailing edge is placed at a $\frac{1}{4}$ panel inset in the θ coordinate. The last kinematic control point is located at $x = 1$ for partial *and* supercavitation. The cavity sources in the wake of the foil are then spaced at $\frac{3}{4}$ increments of the wake source panels, which are of constant length equal to the length (in the x coordinate) of the last source panel on the foil. This wake panel length, ΔX_{wake}, was chosen after numerical experimentation whereby ΔX_{wake} was designated to be a constant, C, times the length of the last source panel on the foil. The value of C was varied in the solution and found to have a moderate effect on the convergence rate and more effect on the computation time. For optimum convergence rate with the constraint of reasonable computation time, $C = 1$ was chosen.

For a partially cavitating foil with thickness and camber and discretized with half-cosine spacing, as few as twenty vortex panels are required to give values for cavitation number,

cavity shape, and singularity distributions which are within 10% of the analytic results. For supercavitation, ten vortex panels are sufficient for the same results. Comparison of the computed cavitation number for a partially cavitating flat plate at an angle of attack with constant spacing and with half-cosine spacing is shown in Figure 2.8. The error[2] in cavitation number not only converged faster for half-cosine spacing, but also converged to a much smaller value.

A thorough investigation of the accuracy of the various spacing techniques may be found in the thesis by Corrado in which he considers only partial cavitation. Similar comparisons of numerical and analytical results for supercavitation are provided in figures 2.9 - 2.12. In these figures, only half-cosine spacing is used in the numerical solution, since all other configurations have been abandoned in its favor.

[2]The error is given by abs$\left(\frac{\sigma_N - \sigma_A}{\sigma_A}\right)$. Subscripts: N = Numerical, A = Analytic

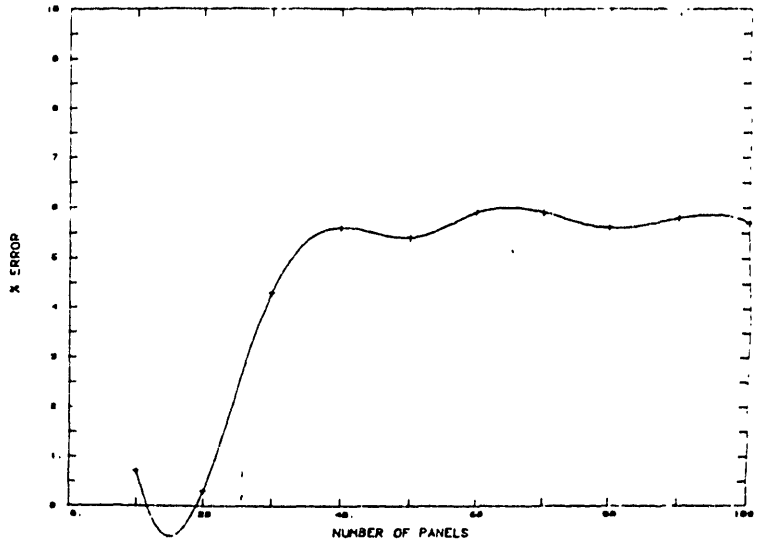

(a)

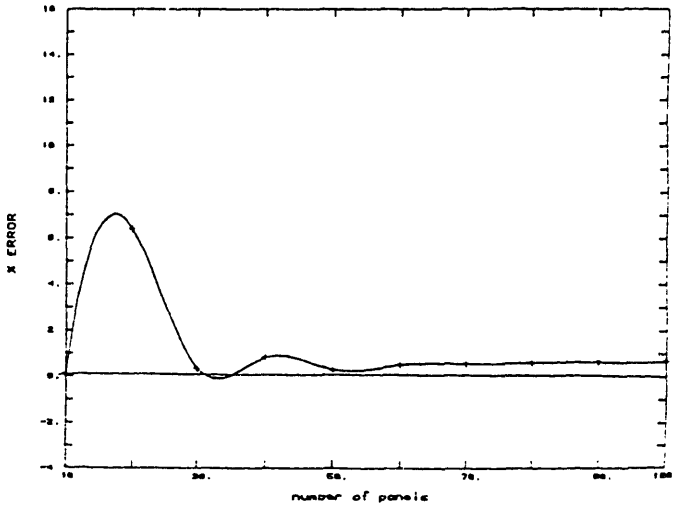

(b)

Figure 2.8: Error in cavitation number for partially cavitating flat plate with (a)constant spacing and (b)half-cosine spacing.

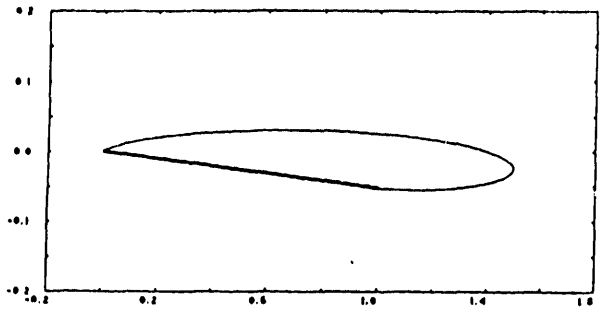

# OF ELEMENTS	NUMERICAL SIGMA	ANALYTICAL SIGMA	NUMERICAL AREA	ANALYTICAL AREA	% ERRORS SIGMA	% ERRORS AREA
5	.1938	.1676	.0797	.0744	15.6	7.0
10	.1460	.1466	.0802	.0821	.50	2.3
20	.1491	.1495	.0795	.0808	.24	1.5
40	.1509	.1510	.0794	.0801	.10	1.0
80	.1482	.1487	.0805	.0811	.35	.71
100	.1482	.1487	.0806	.0811	.35	.64

Figure 2.9: Supercavitating flat plate, l=1.5, $\alpha = 3°$.

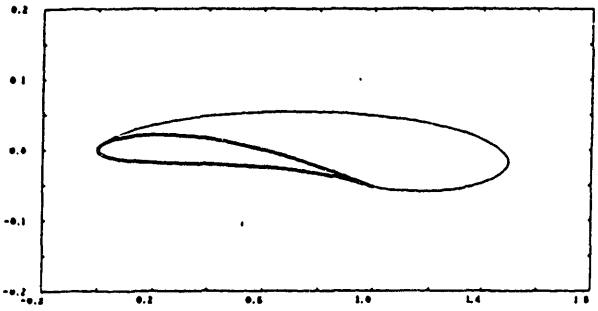

# OF ELEMENTS	NUMERICAL SIGMA	ANALYTICAL SIGMA	NUMERICAL AREA	ANALYTICAL AREA	% ERRORS SIGMA	% ERRORS AREA
5	.3057	.2357	.0988	.0771	30.0	28.1
10	.2082	.2070	.0883	.0872	.60	1.25
20	.2111	.2110	.0852	.0853	.06	.15
40	.2131	.2131	.0843	.0844	0	.14
80	.2095	.2100	.0858	.0858	.20	0 0
100	.2095	.2099	.0859	.0858	.20	.10

Figure 2.10: Supercavitating Joukowski thickness form with parabolic meanline. $\tau_{max} = .04$, $\eta_{max} = .02$, $\alpha = 3°$, $l = 1.5$.

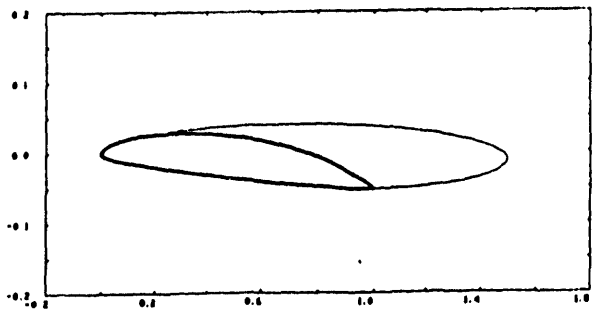

# OF ELEMENTS	NUMERICAL SIGMA	ANALYTICAL SIGMA	NUMERICAL AREA	ANALYTICAL AREA	% ERRORS SIGMA	% ERRORS AREA
5	.1538	.1645	.0502	.0504	6.5	.40
10	.1392	.1423	.0570	.0581	2.1	2.0
20	.1385	.1453	.0538	.0567	4.7	5.1
40	.1416	.1469	.0538	.0560	3.6	4.0
80	.1420	.1445	.0561	.0571	1.7	1.7
100	.1423	.1445	.0563	.0571	1.5	1.3

Figure 2.11: Supercavitating NACA 16 thickness form with NACA a=.8 camber. τ_{max}=.06, η_{max} = .02, $\alpha = 3°$, $l = 1.5$.

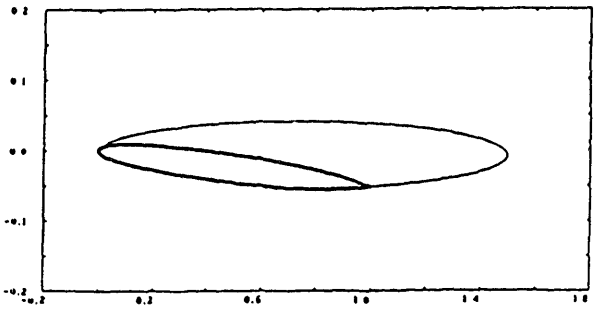

# OF ELEMENTS	NUMERICAL SIGMA	ANALYTICAL SIGMA	NUMERICAL AREA	ANALYTICAL AREA	% ERRORS SIGMA	% ERRORS AREA
5	.1475	.1467	.0695	.0709	.51	1.9
10	.1306	.1256	.0768	.0782	4.0	1.8
20	.1268	.1284	.0747	.0769	.30	2.8
40	.1293	.1299	.0747	.0762	.43	2.1
80	.1279	.1276	.0767	.0772	.20	.70
100	.1279	.1276	.0769	.0772	.20	.40

Figure 2.12: Supercavitating VLR thickness form at $\alpha = 3°$, τ_{max}=.04, ρ_{LE}=.001613, $l = 1.5$.

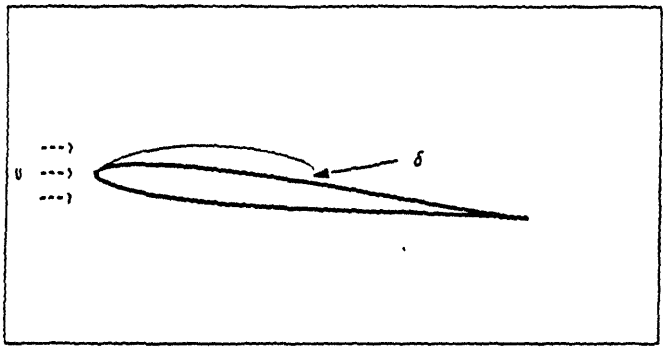

Figure 2.13: Open cavity model

2.3.3 Open Cavity Model

The numerical model for partial cavitation has been modified to allow for a small cavity wake thickness δ (normalized on chord length) by replacing the cavity closure condition (2.31) with the cavity "non-closure" condition:

$$\sum_{i=1}^{M} Q_i = \delta. \tag{2.40}$$

The open cavity model is motivated almost exclusively by experimental observations in which partial cavities develop a wake of nearly constant thickness, equal to the thickness of the cavity at its trailing edge (see Figure 2.13). This linearized open cavity model is due to Fabula [4], and was implemented in the analytical solution by Kinnas. However, open wake models have also been considered in the non-linear solution [18], motivated by the desire to simulate the ultimate wake defect and to obtain a better estimate of the drag.

The numerical solution is sensitive to the cavity wake thickness δ. Figure 2.14 is a parametric plot of σ vs N (number of vortex panels) for a partially cavitating flat plate for various cavity wake thicknesses. In this figure, numerical results are compared to analytical results showing that:

1. $\Delta\sigma \propto \delta$ and $\Delta\sigma < 0$
2. the numerical results diverge for increasing δ.

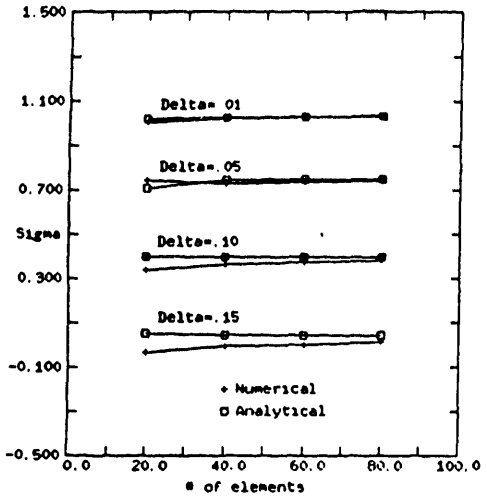

Figure 2.14: Numerical and Analytical results for a flat plate with varying δ.

The latter result is due to the misrepresented singularity in the cavity source distribution at the trailing edge of the cavity. Recall that the discrete sources are placed at points, relative to the panel boundaries, which best model the square-root singularity in q due to the large slope at the cavity's trailing edge. For an open cavity, this slope is smaller at the trailing edge; however, the strength of the square-root singularity in q is not adjusted. Figure 2.14 shows that the results are good for small δ and increasingly inaccurate for larger δ.

Chapter 3 will discuss the results of an experiment in which the thickness of the wake is measured for several cavity lengths. It is fortunate that δ is observed to be small ($O(10^{-3})$) so that the numerical and experimental results may be compared without further modifications of the numerical method.

2.4 Application

The tools developed for the analysis of flow around cavitating two dimensional hydrofoils are very useful for determining the lift and drag characteristics for a given hydrofoil and cavity length. For example, the following are results for the NACA 16006 symmetric foil for angles of attack varying from 1 to 5 degrees and σ between .05 and .25, corresponding roughly to

cavity lengths between 1.5 and 3.0 chord lengths:

1. cavity length vs. σ (Figure 2.15)
2. cavity area vs. σ (Figure 2.16)
3. lift coefficient vs. σ (Figure 2.17)
4. drag coefficient vs. σ (Figure 2.18)
5. lift/drag ratio vs. σ (Figure 2.19)
6. cavity plots for a chosen cavity length for each angle of attack. (Figure 2.20)

In the course of this research, cambered foils were analyzed for angles of attack varying from -5° to +5° and σ between .05 and .30 (or cavity lengths from 1.5 to 4.0). To obtain results for the negative angles of attack, it was noticed that the flow around a cambered foil at a negative angle of attack is identical to the flow around the foil at a positive angle of attack with inverted camber. This can be seen in Figure 2.21, where the results are shown for a NACA 66 foil at -3°. Since the cavity plot is the only result of the analysis which depends on the orientation, all other results (lift, drag, etc.) are correct. The "true" cavity can be seen by simply inverting the plot.

It was necessary to find the correct detachment point on the lower side of the foil (labeled X_s in Figure 2.21) to complete the analysis. This is also a necessity for thick symmetric foils at small angles of attack, as can be seen in Figure 2.20. The case where cavity detachment on the pressure side of the foil occurs forward of the trailing edge is called "face" cavitation. The analysis for including face cavitation in the results is described in Chapter 4.

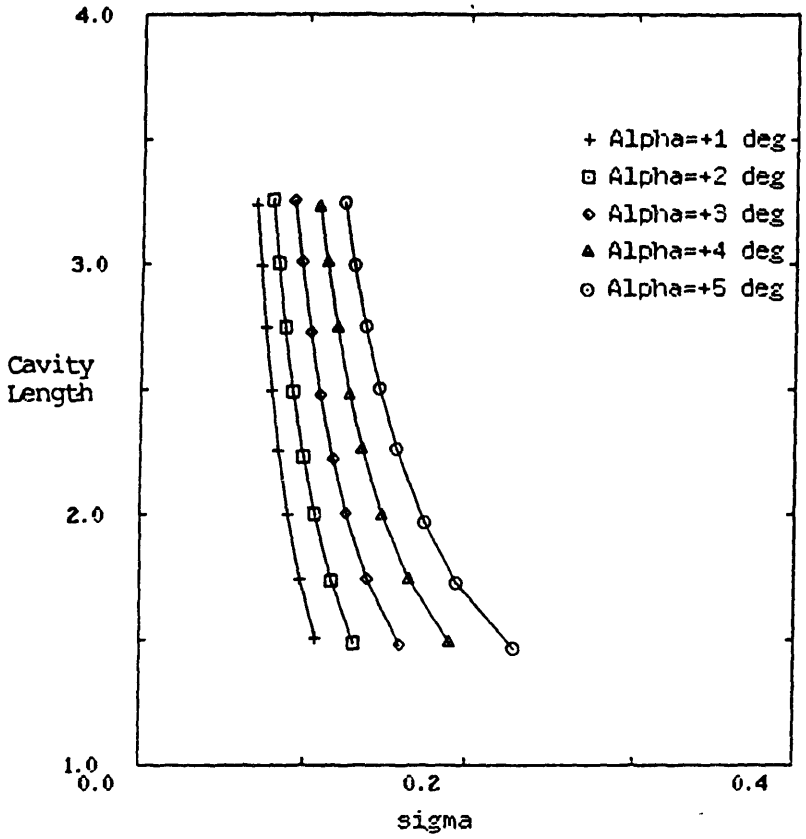

Figure 2.15: Cavity length vs. σ for varying angle of attack for NACA 16006 symmetric foil.

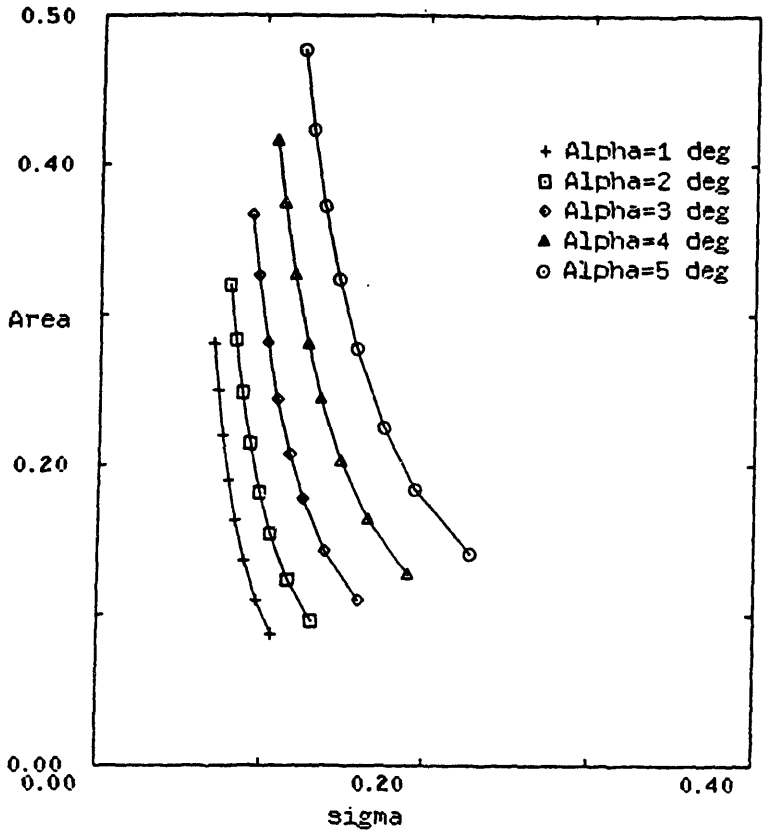

Figure 2.16: Cavity area vs. σ for varying angle of attack for NACA 16006 symmetric foil.

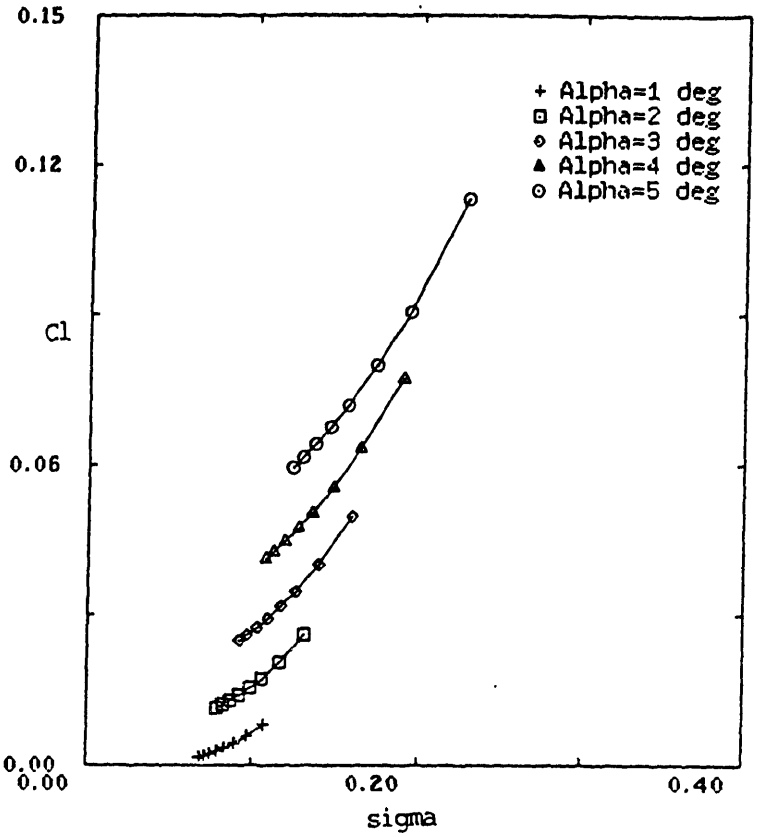

Figure 2.17: Lift coefficient vs. σ for varying angle of attack for NACA 16006 symmetric foil.

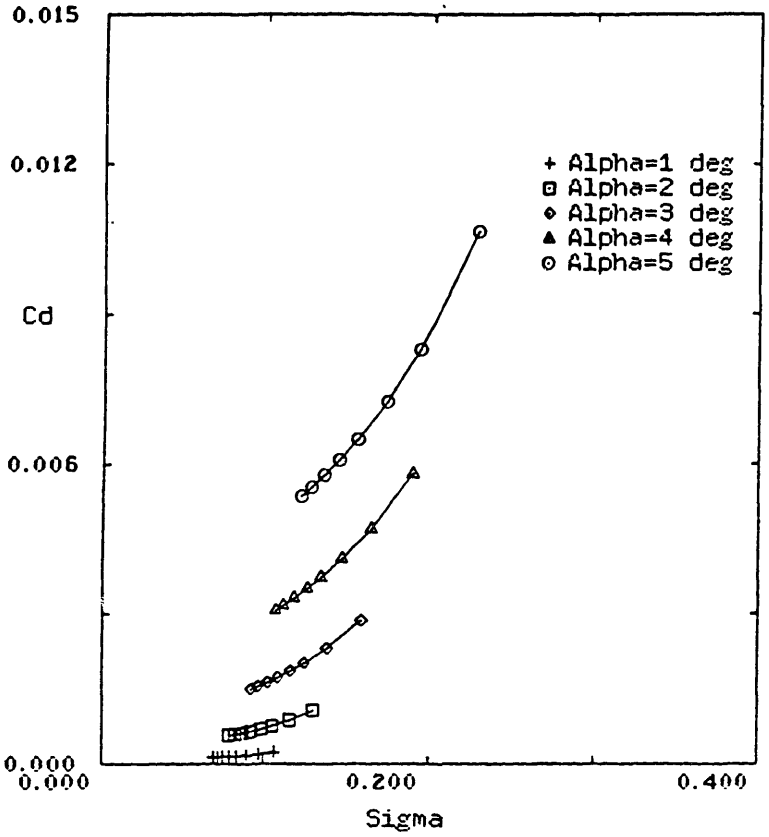

Figure 2.18: Drag coefficient vs. σ for varying angle of attack for NACA 16006 symmetric foil.

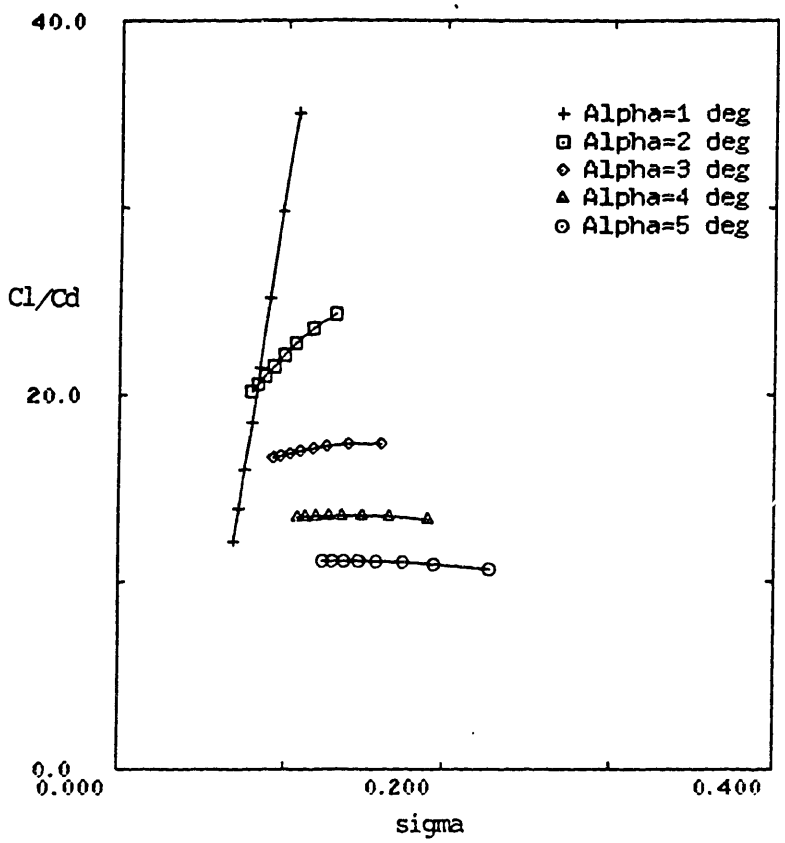

Figure 2.19: Lift/Drag ratio vs. σ for varying angle of attack for NACA 16006 symmetric foil.

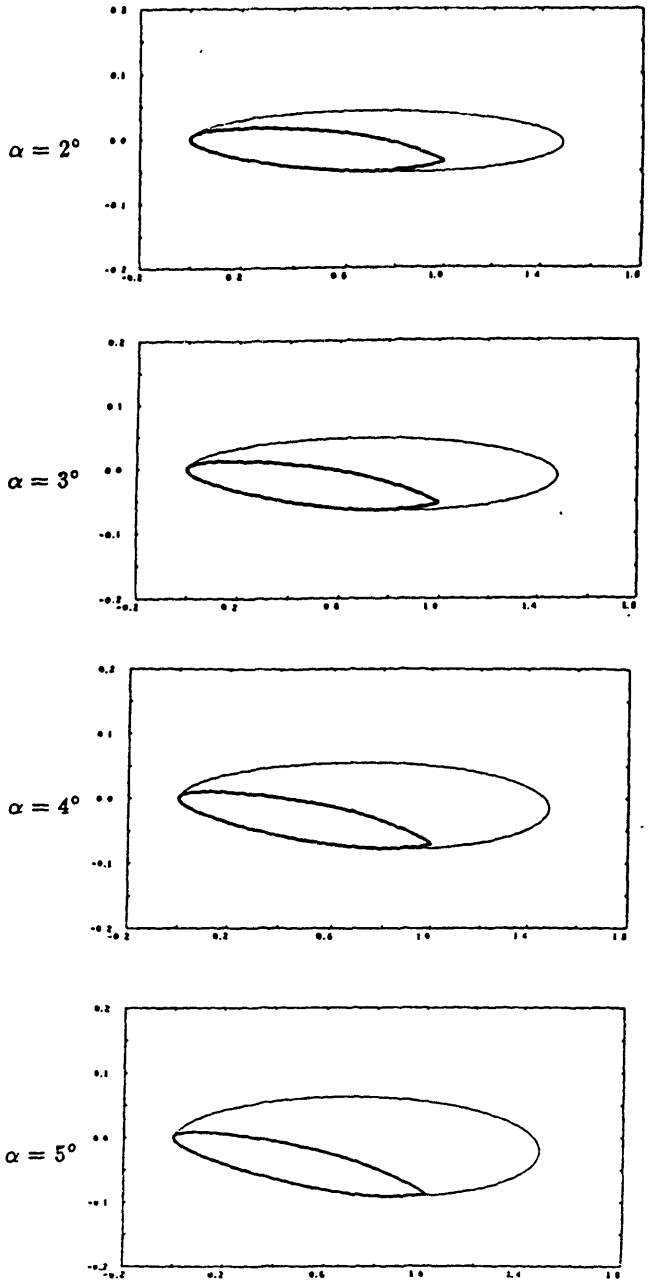

Figure 2.20: Cavity plots for $l = 1.5$ at each angle of attack for NACA 16006 symmetric foil.

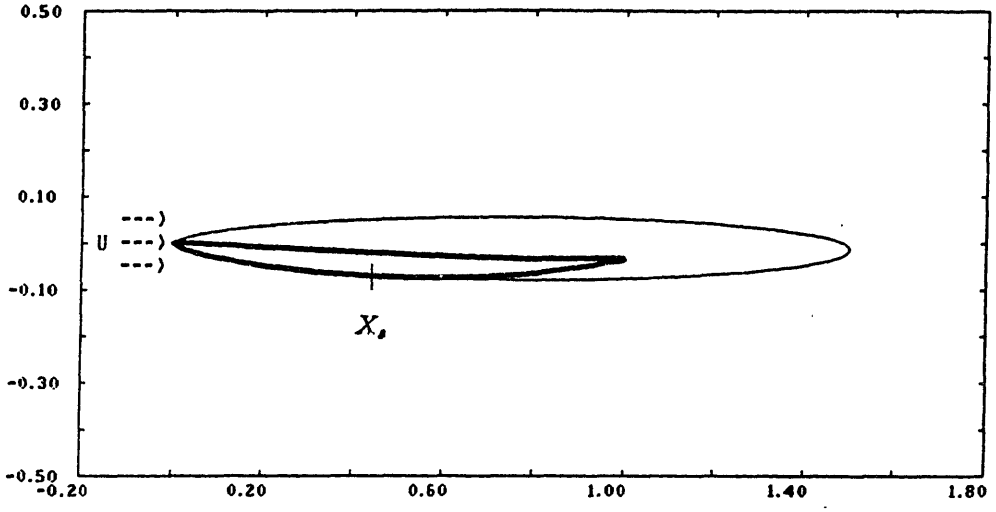

Figure 2.21: Cavity plot for cambered foil at -3° angle of attack. NACA 66 thickness profile (τ_{max}=.04), NACA a=.8 meanline (η_{max}=.03).

Chapter 3

Experimental Considerations

3.1 Introduction and Motivation

The development of analytical and numerical methods for solving the partial and supercavitating hydrofoil problem in two dimensions was described in the previous chapter. One goal was to compare results from the discrete singularities method to the semi-analytical results of Kinnas [11]. In this chapter, the goal is to compare numerical predictions of cavitation number to experimental measurements and to determine the thickness of the cavity wake.

An experiment was performed in the Variable Pressure Water Tunnel of the MIT Marine Hydrodynamics Lab with the following objectives:

1. To compare measured cavitation numbers for various cavity lengths to those predicted by the analytical and numerical models.

2. To investigate the velocity profiles above and behind the cavities and to estimate the displacement thickness behind the cavity for comparison with the measured displacement thickness of the non-cavitating foil.

This stage of the research was completed in two steps. First, velocity profiles were measured in vertical planes at various stations on and behind the cavities and integrated to obtain displacement thicknesses. The pressure distribution was calculated on the suction side of the noncavitating foil for use in finding an effective angle of attack accounting for the viscous boundary layer. Second, the numerical code was modified to account for the tunnel wall effect in order to facilitate appropriate comparisons.

This chapter will describe these two steps and their results.

3.2 Setup

The Marine Hydrodynamics Lab test hydrofoil #3[1] was mounted in the test section of the MIT variable pressure water tunnel (see Figure 3.1). This foil has the following characteristics:

- VLR (Variable Leading edge Radius) thickness form[2] ($\tau_{max} = .04$)
- NACA a=.8 meanline ($\eta_{max} = .02$)
- Leading edge radius = .001613
- Trailing edge thickness = .004

It was mounted and secured by a single axis which protrudes through holes in the glass walls of the tunnel test section. Hinges on the outer side of the walls allowed for variation in the angle of attack of the foil with respect to the horizontal inflow.

Thin rubber gaskets were placed between the foil and the inner walls to prevent seepage due to the pressure difference from top to bottom of the foil. Some time was spent trimming the gaskets to prevent interference with the flow and, in particular, to ensure good two dimensionality. A thin layer of RTV was applied to the top of the gaskets to fill gaps and to harden the surface.

Free stream velocity was kept approximately constant throughout the experiment at 22.5 ft/sec, corresponding to a Reynolds number based on chord length of 3.1×10^6. Change in cavity length and σ was accomplished by varying the water pressure.

The cavities were observed to be very two dimensional with length oscillating about some mean. The period of the oscillations grew as the cavity length increased until, for cavity lengths greater than 60% chord, the cavities became very unstable.

[1]Provided courtesy of Bird-Johnson Co.
[2]Designed by Professor J.E. Kerwin of the Department of Ocean Engineering, MIT

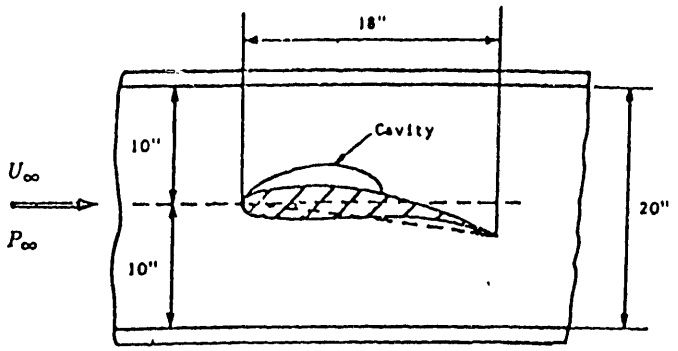

Side View

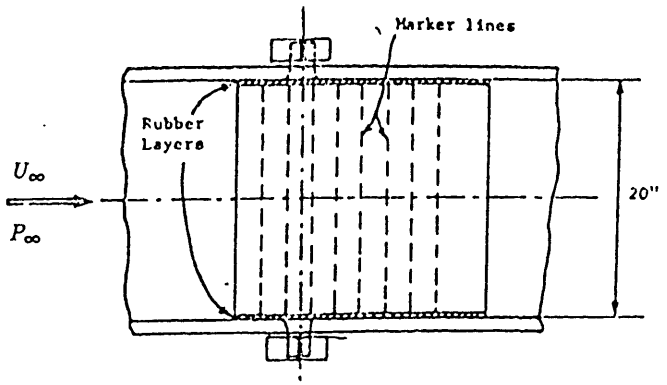

Top View

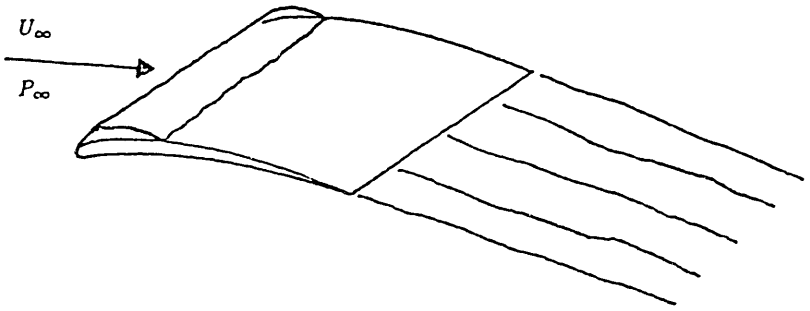

Figure 3.1: Experiment geometry

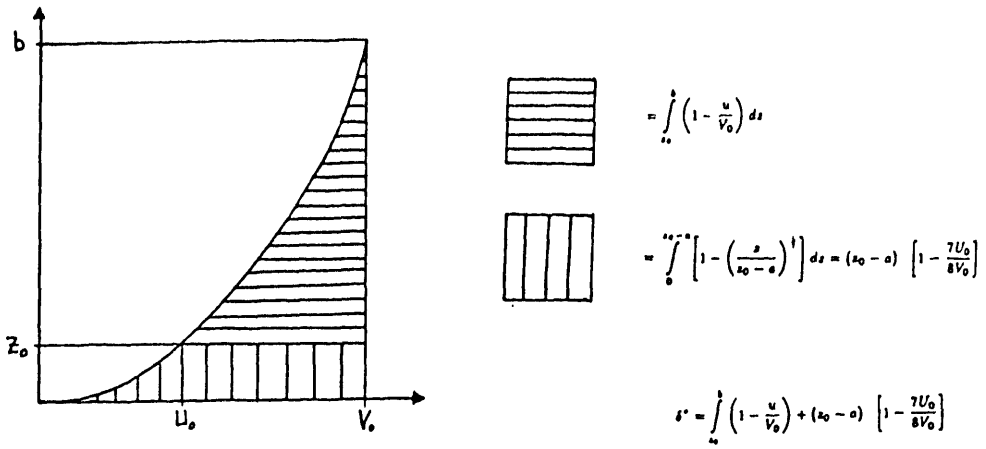

Figure 3.2: Graphic computation of cavity wake thickness δ.

Velocity profiles above and behind the cavities were measured with the Laser Doppler Velocimeter (LDV), which calculates an "instantaneous" velocity by counting particles in the water as they cross interference fringes. Only the horizontal velocity was measured since one of the two laser beams used in the measurement of vertical velocity was blocked by the hydrofoil.

3.3 Results

3.3.1 Cavity Wake Thickness

Horizontal velocity profiles were measured for cavity lengths of 10%, 20%, 30%, and 40% chord at stations located at approximately 10%, 40%, 60%, 70%, and 80% chord. Measurements beyond 80% chord were prohibited by the limitations of the apparatus. Also, measurement between 15% and 35% chord was impossible due to the obstruction of the mounting hinges. Figure 3.3 shows velocity profiles for a 10% cavity[3]. Each plot in this figure includes profiles for cavitating and non-cavitating foils together so that the cavity wake may be compared to the non-cavitating boundary layer. Similar results for cavity lengths of 20%, 30%, and 40% are shown in Figures 3.4 - 3.6.

[3]A 10% cavity is one with length equal to 10% of the chord length.

From these velocity profiles, the displacement thicknesses are determined for cavitating and non-cavitating foils by numerical integration of the raw data. The cavity wake thickness is defined as

$$\delta = \delta_c^* - \delta_{nc}^* \tag{3.1}$$

where, in general, the displacement thickness is defined as

$$\delta^* = \int_0^\infty \left(1 - \frac{u}{U_\infty}\right) dy. \tag{3.2}$$

The results shown in Table 3.1 indicate a nearly constant wake thickness for each cavity length. Note, however, that the wake thickness shows greater variations for larger cavity lengths. This behavior may be caused by the unsteady nature of the larger cavity.

Displacement thickness was calculated using a trapezoidal integration of the raw data and adding a small correction for the thin viscous boundary layer where velocity measurements were not possible. The correction was a simple application of the $\frac{1}{7}$ power law, as described by Newman [14]. Figure 3.2 shows graphically how the displacement thickness was calculated from the experimental data.

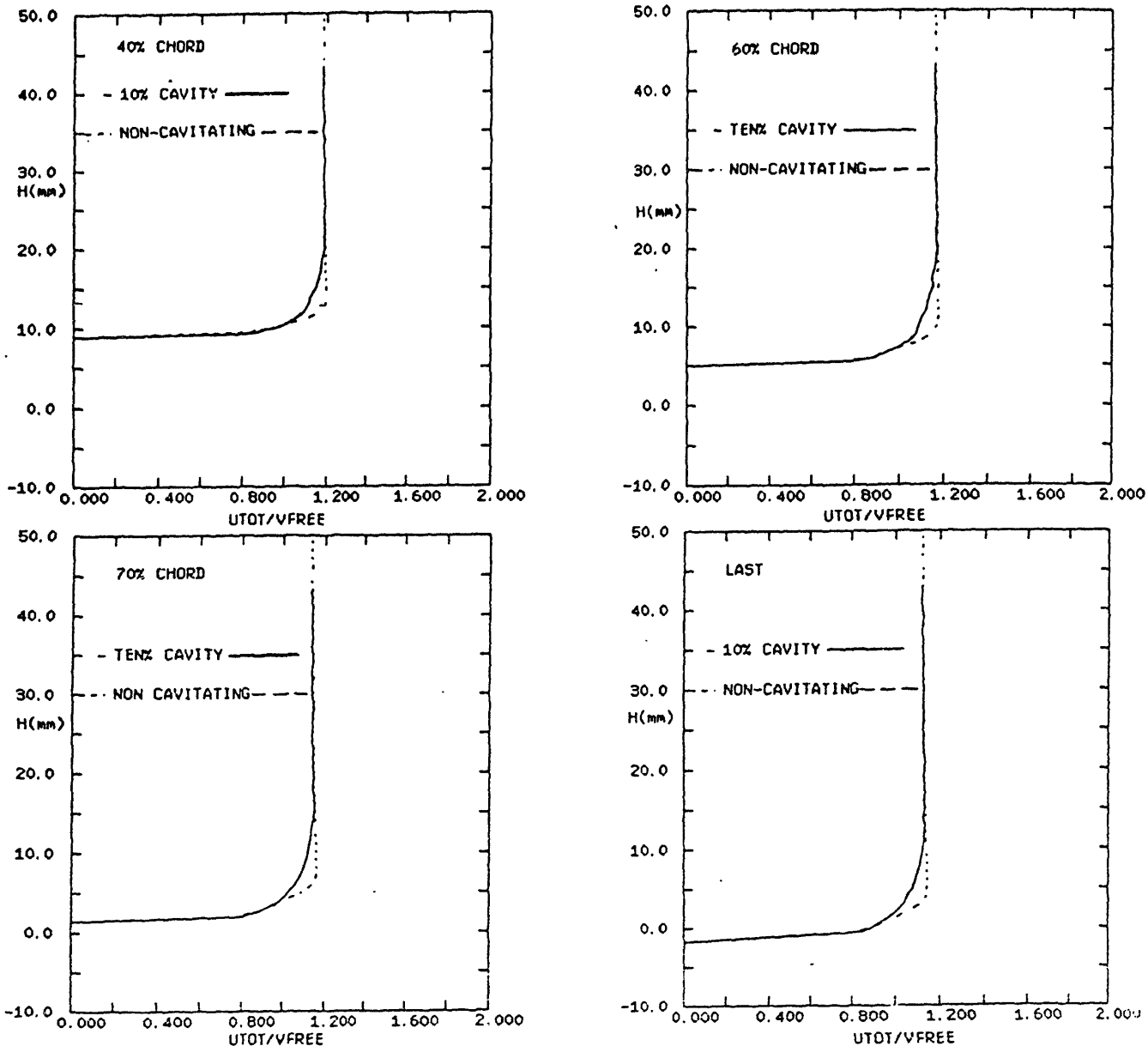

Figure 3.3: Velocity profiles behind a 10% cavity.

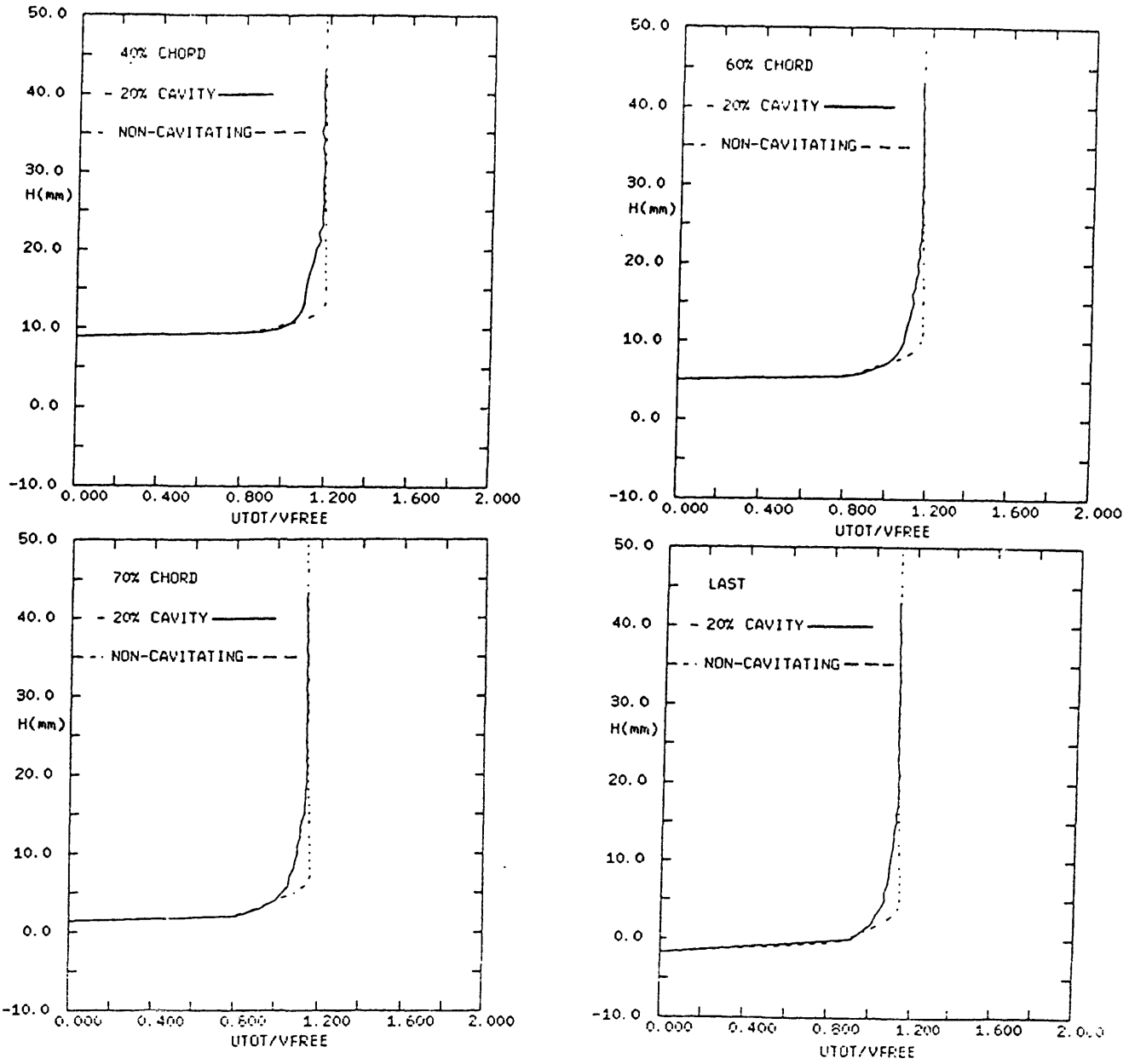

Figure 3.4: Velocity profiles behind a 20% cavity

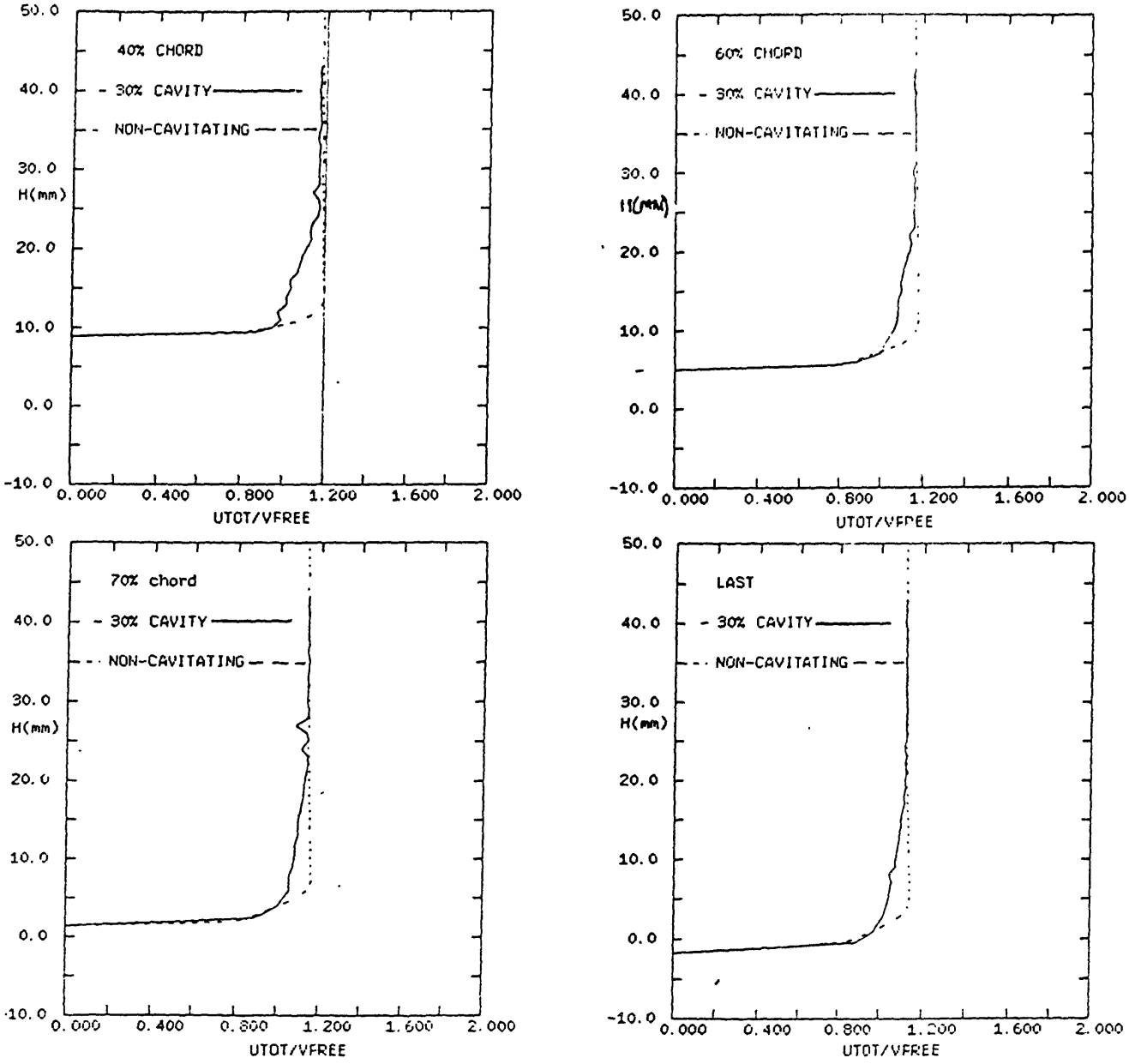

Figure 3.5: Velocity profiles behind a 30% cavity

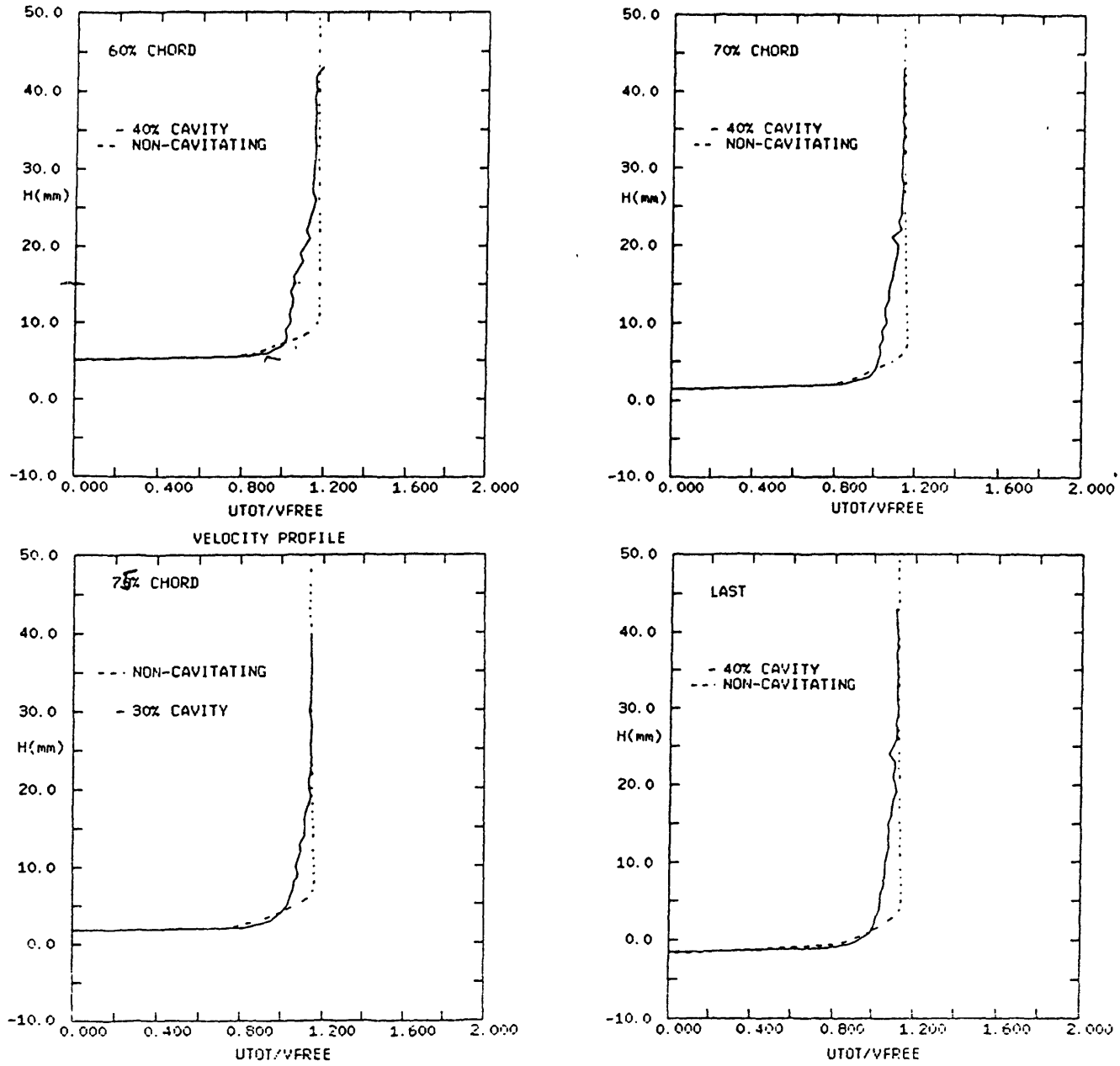

Figure 3.6: Velocity profiles behind a 40% cavity

% Chord	Wake Thickness	% Deviation From Mean
	10% cavity	
41.2	6.926e-04	-.73
60.1	7.334e-04	5.22
70.2	7.168e-04	2.77
76.6	6.473e-04	-7.19
	20% cavity	
41.2	9.988e-04	4.57
60.1	1.016e-03	6.36
70.2	8.538e-04	-10.60
76.6	9.519e-04	-.30
	30% cavity	
41.2	1.895e-03	23.60
60.1	1.347e-03	12.1
70.2	1.467e-03	-4.3
76.6	1.420e-03	-7.3
	40% cavity	
60.1	2.071e-03	19.76
70.2	1.739e-03	.55
73.5	1.268e-03	-26.70
76.6	1.839e-03	6.4

Table 3.1: Cavity wake thickness

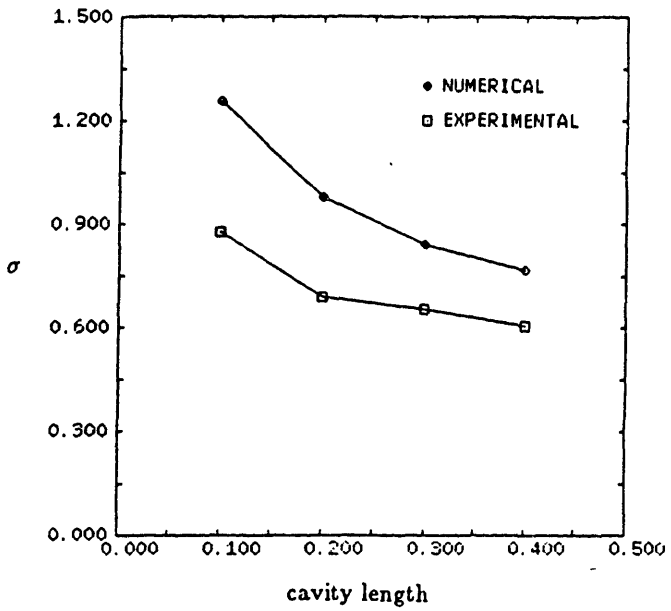

Figure 3.7: Cavitation number vs. cavity length; numerical and experimental results.

3.3.2 The Cavitation Number

Figure 3.7 is a plot of the cavitation number vs. cavity length for the four cavity lengths measured. Superimposed on the experimental results are the numerical results from the method of discrete singularities. Since the numerical results represent the solution to the *linearized* boundary value problem of the *two dimensional*, partially cavitating hydrofoil in *inviscid, incompressible, irrotational, steady, unbounded* flow with *closed cavity*, the difference between the two curves must be a weighted combination of the following factors:

1. non-linear effects
2. three dimensional effects
3. real fluid effects
4. boundedness of the flow

5. open cavity
6. unsteady effects
7. inaccuracy of the numerical method

Assuming that the flow was two-dimensional enough and steady enough to satisfy the conditions of the numerical solution, the following four corrections are proposed:

1. implementation of the open cavity model, with δ determined from experiment
2. Lighthill's leading edge correction to the cavitating solution
3. approximation of the effect of the boundary layer
4. method of images to account for the presence of the tunnel walls.

With these four corrections to the numerical solution, comparison with experimental results is then a gauge of the accuracy of the numerical method. Each of these corrections will be considered in turn and the final correlation will be presented.

Open cavity model

The open cavity model was discussed in section 2.3.2. The cavitation number can be shown to decrease by an amount proportional to δ. Since the measured δ was small, the effect on the cavitation number is expected to be only a small perturbation.

Leading edge corrections

Linear theory incorrectly predicts that increasing the foil thickness, while maintaining otherwise identical flow conditions, results in larger cavity volumes. This has been shown [20] to be due to the failure of linear theory to account for a varying horizontal perturbation velocity on the surface of the cavity near the leading edge. However, by incorporating Lighthill's leading edge correction in the linear solution, the proper behavior of cavity shape with changes in the foil thickness is observed. For details, see Kinnas [16].

Boundary layer correction

The effect of the boundary layer on a non-cavitating hydrofoil is to modify the free-streamline flow around the foil, effectively changing its shape. That is, the potential flow

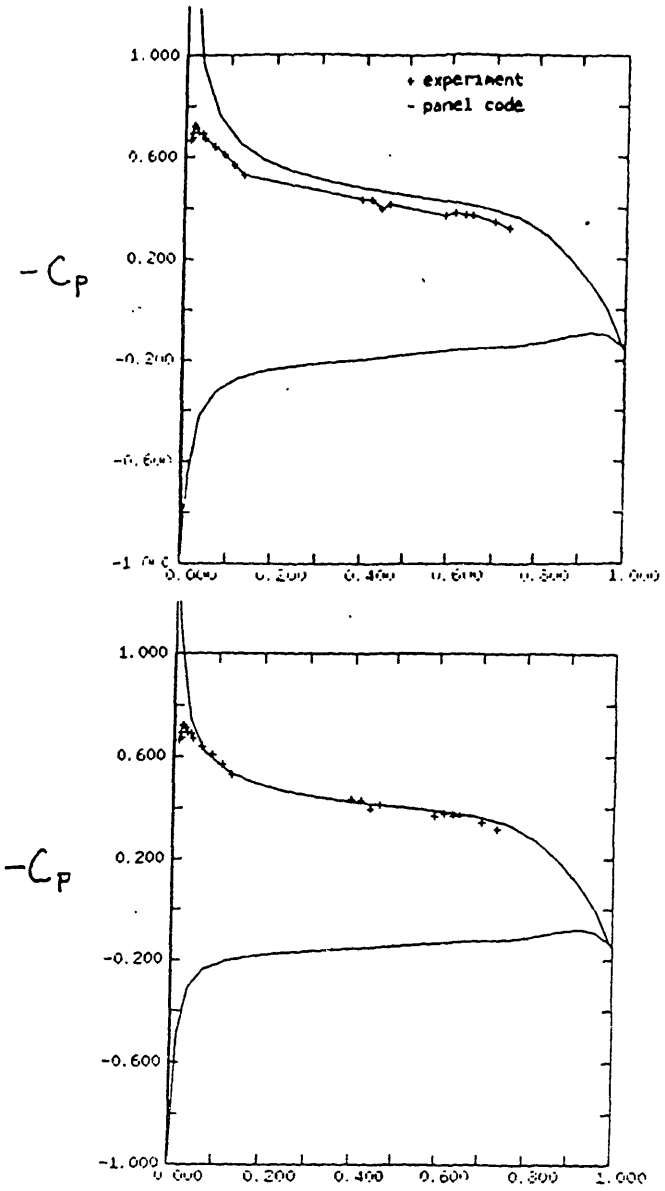

Figure 3.8: Comparison of pressure distributions measured on the suction side of the experiment foil to the computed results. The effective angle of attack, for which the two curves match, accounts for the effect of the boundary layer.

Pinkerton's Results:	α_0	0°	2°		4°	8°	12°
	α_{eff}	−.5°	1.2°		2.9°	6.4°	10.0°
Current Results:			α_0	2.6°			
			α_{eff}	1.9°			

Table 3.2: Effective angle of attack for various geometric angles

can be considered to be confined to the region outside of the area defined by the foil plus the displacement thickness. The effect of the boundary layer is thus *seen* as a small change in the hydrofoil shape and angle of attack. To compute these changes exactly would require the tedious measurement of the displacement thickness all around the hydrofoil. However, Pinkerton [15] found that the calculated and measured pressure distributions for a NACA 4412 airfoil could be brought into agreement by use of an effective angle of attack to account for the boundary layer. The effective angle of attack is smaller than the actual ("geometric") angle of attack, since the displacement thickness on the upper foil surface is larger than that on the lower surface.

To find the effective angle of attack, an existing panel code[4] was modified to include the effect of the tunnel walls (via the method of images). The resulting pressure distribution for the experimental geometry was compared to the measured pressure distribution on the suction side of the non-cavitating foil (Figure 3.9). The angle of attack was then adjusted in the panel code computation until the two curves matched. Note that the measured pressure distribution is computed from the *horizontal* velocity rather than the total velocity; thus it is accurate only where the foil slope is small. This accounts for the discrepancy at the leading edge.

Table 3.2, borrowed from Babeau and Latorre [1], shows Pinkerton's results for the effective angle of attack at various geometric angles for the NACA 4412 foil and Reynolds number of 3.0×10^6. Below this table is shown the current effective angle of attack at $Re = 3.1 \times 10^6$ for the foil geometry described in section 3.2. It is interesting to note that the current results fit

[4]The potential-based panel method is discussed in the thesis by J.T. Lee. The code was written by Lee in the course of his research at MIT.

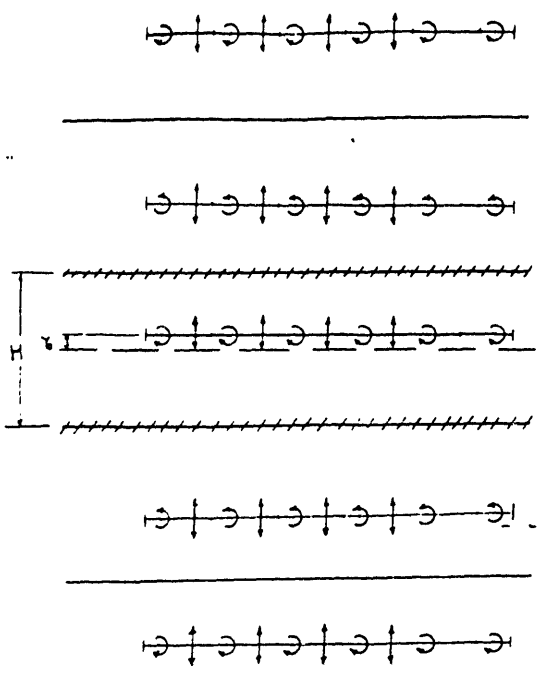

Figure 3.9: Method of images for discrete singularities, accounting for the presence of the tunnel walls.

in well with the previous results despite the difference in foil geometry.

Tunnel walls

The kinematic boundary condition on the tunnel floor and ceiling, the condition that there be no velocity component normal to the surface, may be approximated by placing a finite number of image singularities symmetrically about the tunnel walls (Figure 3.9). By the *method of images,* the kinematic boundary condition is met exactly with an infinite number of images. However, in this work it was found that as few as four or five images on either side of the tunnel is sufficient for the vertical velocity at the tunnel walls to vanish to $O(10^{-4})$.

The kinematic and dynamic boundary conditions (2.26, 2.27) are modified to include the velocity induced by the images:

1. *Kinematic boundary condition*

$$\begin{aligned} LHS\ of\ 2.26 \ + \ & \sum_{j=1}^{N_{images}} \left[\frac{1}{2\pi} \sum_{i=1}^{KT} \frac{d\tau}{dx} \frac{h}{(X_{\tau_i} - X_k)^2 + h^2} \right] = \\ RHS\ of\ 2.26 \ + \ & \sum_{j=1}^{N_{images}} \left[(-1)^j \frac{1}{2\pi} \sum_{i=1}^{N} \frac{\Gamma_i (X_{v_i} - X_k)}{(X_{v_i} - X_k)^2 + h^2} \right] \\ + \ & \sum_{j=1}^{N_{images}} \left[\frac{1}{2\pi} \sum_{i=1}^{M} \frac{Q_i (X_k - X_{s_i})}{(X_{s_i} - X_k)^2 + h^2} \right] \end{aligned} \tag{3.3}$$

2. *Dynamic boundary condition*

$$\begin{aligned} LHS\ of\ 2.27 \ + \ & \sum_{j=1}^{N_{images}} \left[\frac{1}{2\pi} \sum_{i=1}^{KT} \frac{d\tau}{dx} \frac{(X_{\tau_i} - X_d)}{(X_{\tau_i} - X_d)^2 + h^2} \right] = \\ RHS\ of\ 2.27 \ + \ & \sum_{j=1}^{N_{images}} \left[(-1)^j \frac{1}{2\pi} \sum_{i=1}^{N} \frac{\Gamma_i (-h)}{(X_{v_i} - X_d)^2 + h^2} \right] \\ + \ & \sum_{j=1}^{N_{images}} \left[\frac{1}{2\pi} \sum_{i=1}^{M} \frac{Q_i (X_d - X_{s_i})}{(X_d - X_{s_i})^2 + h^2} \right] \end{aligned} \tag{3.4}$$

The final correlation of the experimental and numerical cavitation numbers, Figure 3.10, shows excellent agreement, in support of the accuracy of the numerical method.

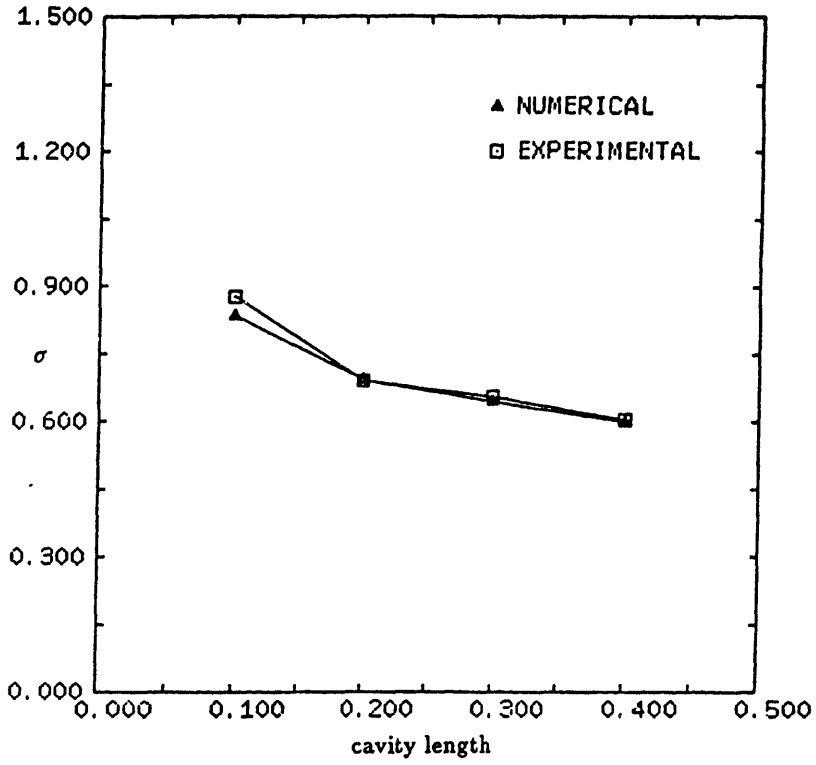

Figure 3.10: Final correlation between experimental and numerical cavitation numbers

Chapter 4

Midchord Detachment and Face Cavitation

4.1 Introduction

It has been observed that some propellers cavitate at design conditions with the cavities detaching aft of the leading edge on the suction side and/or forward of the trailing edge on the pressure side of the foil. The former is referred to as "midchord detachment" and the latter as "face cavitation". Thus, there are in general four independent ways in which a foil may supercavitate (see Figure 4.1). For each case, the boundary conditions differ, and the solutions must be considered separately. In Figure 4.1, case (a) has been solved previously (section 2.1.2). Cases (b) through (d) contain face cavitation and/or midchord detachment, and their solution is necessary to make the analysis tool complete. In this chapter, these cases are developed analytically and a method for predicting the cavity detachment points is described.

4.2 Face Cavitation

For thick symmetric foils at small angles of attack and for many foils at negative angles of attack, it is found that the supercavity detaches forward of the trailing edge on the pressure side of the foil (Figure 4.2). The point of separation, X_s, may be found by considering the following two conditions:

1. the pressure on the wetted foil surface must be greater than the cavity pressure
2. the cavity and foil surface must not intersect aft of the separation point.

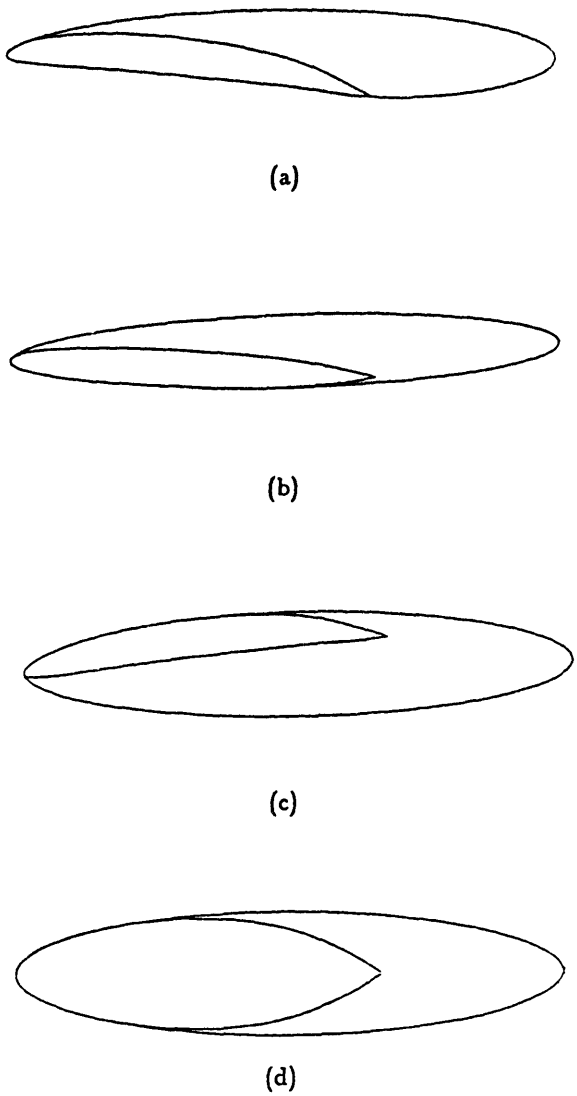

Figure 4.1: Four forms of supercavitation: (a)cavity detachment at leading and trailing edges; (b)face cavitation; (c)face cavitation for foil at a negative angle of attack; (d)midchord detachment and face cavitation.

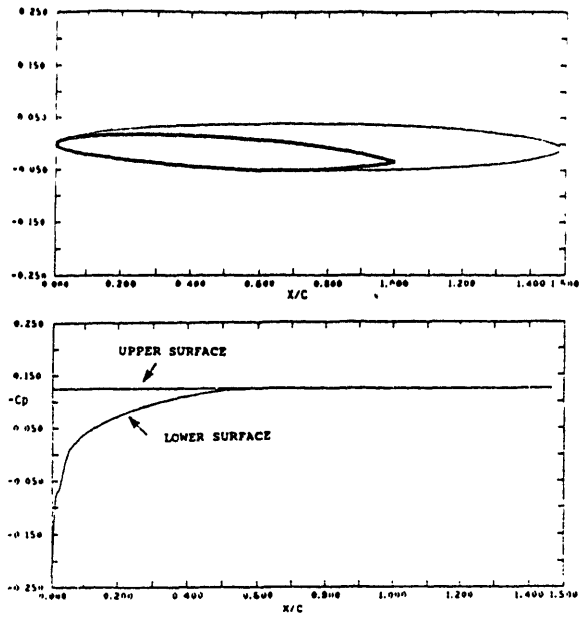

Figure 4.2: Supercavity detachment on the pressure side of a thick symmetric hydrofoil. NACA 66 thickness form $\tau_{max} = .10$, $\alpha = 3°$. Cavity detaches at $\frac{x}{c} = .51$. Below is pressure distribution $-C_p(x)$.

In linear theory, condition 1 is equivalent to

$$\gamma(x) > 0 \qquad for \;\; 0 < x < X_s$$

The behavior of the vorticity near the separation point may be written

$$\gamma(x) \sim A(X_s, l)\sqrt{X_s - x}$$

where A depends only on the point of separation and the length of the cavity (for details, see [17]).

$$\begin{aligned} A(X_s, l) \;=\; & -\frac{\pi}{2\sqrt{2}r^2} \cdot \frac{1}{1+z^2}\left[\sqrt{r^2-1} + z\sqrt{r^2+1}\right] + \int_0^t \sqrt{\frac{\eta}{t-\eta}} \cdot \frac{\Theta^*(z) - \Theta^*(\eta)}{(z-\eta)(1+\eta^2)} d\eta \\ & + \Theta^*(z)\frac{\pi}{\sqrt{2}r^2} \cdot \frac{1}{1+z^2}\left[\sqrt{r^2+1} - z\sqrt{r^2-1}\right] \end{aligned}$$

where

$$z = \sqrt{\frac{x}{l-x}}; \quad t = \sqrt{\frac{1}{l-1}}; \quad r^2 = \sqrt{1+t^2} \tag{4.1}$$

and

$$\Theta^* = \frac{1}{\sigma}\frac{d\eta_l}{dx}. \tag{4.2}$$

By observing the behavior of the vorticity distribution for perturbations about X_s, we conclude that the correct vorticity distribution goes to zero at X_s with zero slope. This can be seen in Figures 4.3 and 4.4, where the leftmost detachment point is positive for $0 < x < X_s$, thereby satisfying the first requirement; however, for this detachment point, the cavity cuts the foil. For the rightmost detachment point, the cavity does not cut the foil, but the requirement of positive vorticity is not satisfied. Clearly, the correct detachment point is somewhere between these two, and the one which satisfies both requirements is the one for which the vorticity is tangent to zero at X_s. At this point, the expression $A(X_s, l)$ vanishes. This condition is sufficient for the determination of the separation point, utilizing a Newton-Raphson (secant method) iterative solver. A typical case requires about five iterations, depending on the accuracy of the initial guesses.

Figure 4.3 shows the vorticity distributions for three different values of X_s, corresponding to the three cavity plots in Figure 4.4. Only one of the cavity detachment points is the correct one; Figure 4.3 shows it is the one for which the vorticity distribution is tangent to the x-axis at X_s.

Once the separation point is found, the new boundary value problem may be solved by rescaling the scaled quantities on X_s. The Kutta condition must be met at X_s, but the solution is otherwise identical to that of the original boundary value problem. As a consequence, the problem of determining X_s is independent of numerical and analytical computations. Therefore, face cavitation results are obtained both numerically *and* analytically.

The same analysis is applied to the case of a supercavitating foil at a negative angle of attack (Figure 4.1b), as discussed in section 2.4.

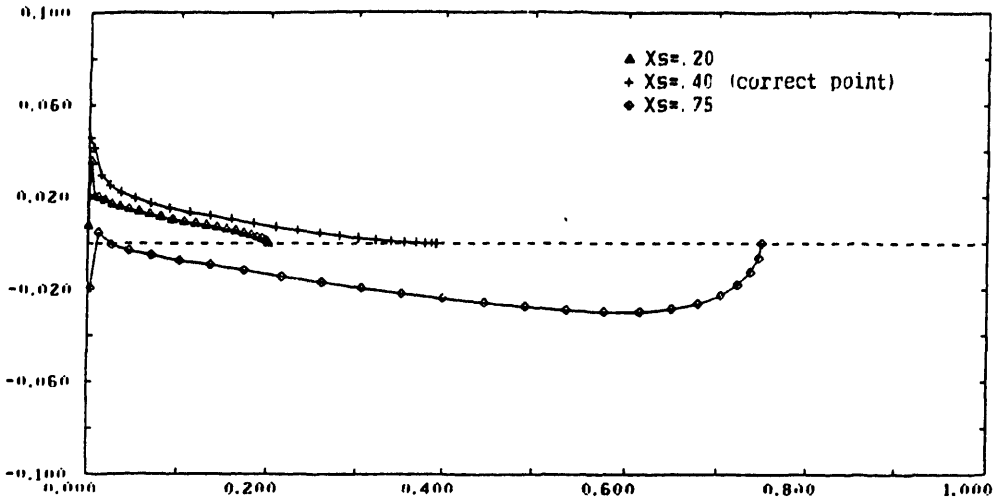

Figure 4.3: Vorticity distributions for three detachment points

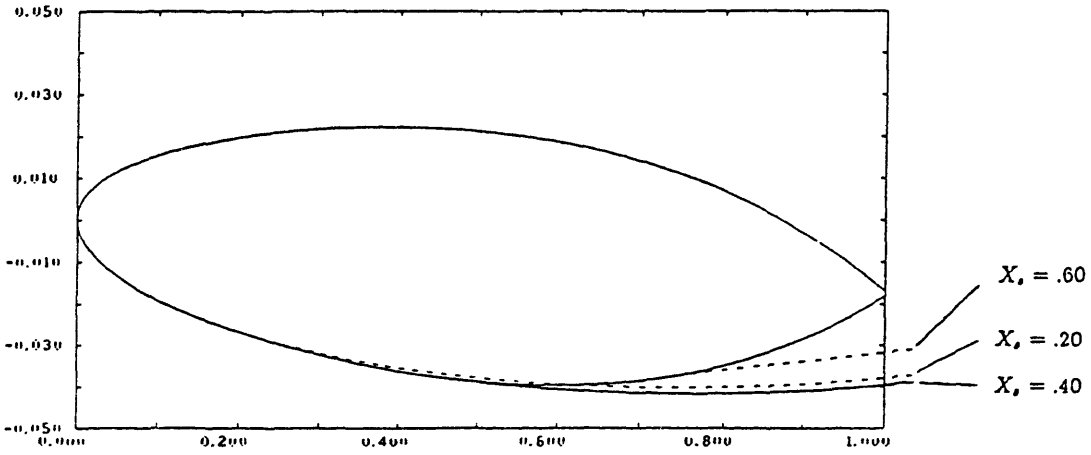

Figure 4.4: Corresponding cavity plots

4.3 Midchord Detachment

4.3.1 Formulation of the Problem

For the case where the supercavity detaches aft of the leading edge on the suction side of the foil (Figure 4.5), the boundary value problem must be modified (for a complete treatment, see Kinnas and Fine [17]). The coupled singular integral equations describing the boundary conditions may be written in the form of equations (2.21, 2.22) with a modified definition of terms. The horizontal perturbation velocity on $y = 0^+$, $u_c^+(x)$, is constant along the cavity but square-root singular on the wetted foil forward of the cavity detachment (Figure 4.6). The dynamic boundary condition may therefore be written

$$u_c^+(x) = \frac{\overline{\gamma}(x)}{2} - \frac{1}{2\pi}\int_0^l \frac{\overline{q}(\xi)d\xi}{\xi - x} \qquad 0 < x < l \tag{4.3}$$

where

$$\overline{\gamma}(x) = \frac{\gamma(x)}{\sigma U_\infty} \tag{4.4}$$

and

$$\overline{q}(x) = \frac{q(x)}{\sigma U_\infty}. \tag{4.5}$$

The kinematic boundary condition becomes

$$\Theta^* = -\frac{\overline{q}}{2} + \frac{1}{2\pi}\int_0^1 \frac{\overline{\gamma}(\xi)d\xi}{\xi - x} \qquad 0 < x < 1 \tag{4.6}$$

with Θ^* as defined in (4.2). Equation 4.6 may be brought into the form of the original kinematic boundary condition (2.21) with the definition

$$\overline{\gamma}^* = \overline{\gamma} - 2(u_c^+ - \frac{1}{2}). \tag{4.7}$$

The new boundary value problem becomes:

1. *Kinematic Boundary Condition*

$$-\frac{\overline{q}}{2} + \frac{1}{2\pi}\int_0^1 \frac{\overline{\gamma}^* d\xi}{\xi - x} = \Theta_2^*(x) \qquad 0 < x < 1 \tag{4.8}$$

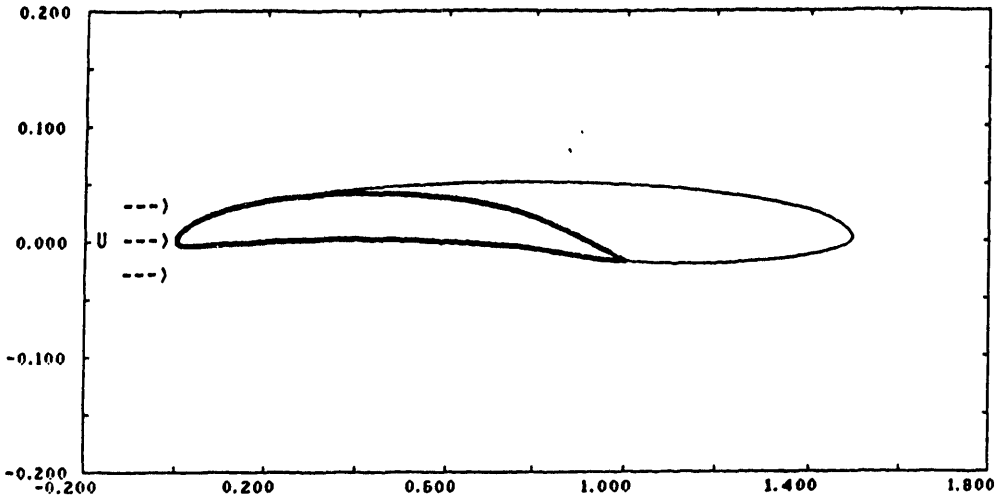

Figure 4.5: Midchord detachment on a supercavitating VLR foil

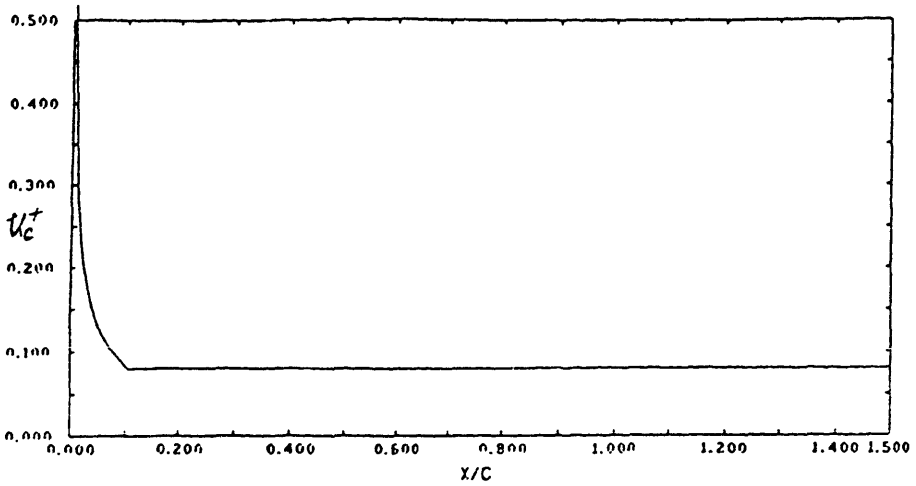

Figure 4.6: Horizontal perturbation velocity on $y = 0^+$

2. *Dynamic Boundary Condition*

$$\frac{\overline{\gamma}^*}{2} - \frac{1}{2\pi}\int_0^l \frac{\overline{q}(\xi)d\xi}{\xi - x} = \frac{1}{2} \qquad 0 < x < l \tag{4.9}$$

3. *Kutta condition*

$$\overline{\gamma}^*(1) = 0 \tag{4.10}$$

4. *Cavity Closure Condition*

$$\int_0^l q(x)dx = 0 \tag{4.11}$$

where we define

$$\Theta_2^* \stackrel{\text{def}}{=} \Theta^* + F \tag{4.12}$$

and

$$F(x) \stackrel{\text{def}}{=} -\frac{1}{\pi}\int_0^{l_0} \frac{u_c^+ - \frac{1}{2}}{\xi - x}d\xi. \tag{4.13}$$

Since this is identical in form to the original boundary value problem described in section 2.1.2, the solution is also identical and is given analytically by Kinnas [11]. Note, however, that the "vorticity" solved for is now $\overline{\gamma}^*$ rather than $\overline{\gamma}$ and the solution for $\overline{\gamma}$, $\overline{q}$, and σ depends on the quantity $u_c^+ - \frac{1}{2}$, which is not known. However, this quantity may be written in terms of integrals of known functions, which are derived by applying the condition that *the source distribution must match the thickness source distribution for* $0 < x < l_0$.

With the transformation of coordinates

$$z = \sqrt{\frac{x}{l-x}}; \quad \omega = \eta = \sqrt{\frac{\xi}{l-\xi}}; \quad t_0 = \sqrt{\frac{l_0}{l-l_0}}; \quad t = \sqrt{\frac{1}{l-1}} \tag{4.14}$$

equation (4.13) becomes

$$F(z) = -\frac{2}{\pi}\cdot(1+z^2)\int_0^{t_0} \frac{(u_c^+ - \frac{1}{2})\omega d\omega}{(\omega^2 - z^2)(1+\omega^2)}. \tag{4.15}$$

Substituting Θ_2^* for Θ^* in equation (16.1a) of Kinnas' PhD thesis, the new source distribution may be obtained:

$$\overline{q}(z) = H(z) - F(z) - \frac{1+z^2}{\pi}\sqrt{\frac{t+z}{z}}\cdot\int_0^t \sqrt{\frac{\omega}{t-\omega}}\frac{F(\omega)d\omega}{(1+\omega^2)(z+\omega)} \qquad z < t \tag{4.16}$$

where

$$H(z) = -\Theta^*(z) + A(z) - \frac{1+z^2}{\pi}\sqrt{\frac{t+z}{z}}\int_0^t \sqrt{\frac{\omega}{t-\omega}}\frac{\Theta^*(\omega)d\omega}{(1+\omega^2)(z+\omega)} \tag{4.17}$$

and

$$A(z) = \sqrt{\frac{t+z}{z}}\cdot\frac{1}{2\sqrt{2}r^2}\cdot\left(\sqrt{r^2-1} - z\sqrt{r^2+1}\right). \tag{4.18}$$

The integral in (4.16) may be simplified by substituting (4.13), reversing the order of integration, and computing the analytic integrals:

$$\begin{aligned}\overline{q}(z) &= H(z) - F(z) \\ &\quad + \frac{2}{\pi}\cdot(1+z^2)\sqrt{\frac{t+z}{z}}\int_0^{t_0}\frac{(u_c^+ - \frac{1}{2})\omega}{(1+\omega^2)(z-\omega)}\left[\frac{1}{z+\omega}\sqrt{\frac{z}{z+t}} - \frac{1}{2\omega}\sqrt{\frac{\omega}{\omega+t}}\right]d\omega.\end{aligned}$$

If we define $\overline{q}_0$ and σ_0 to be the source distribution and cavitation number for the case where the cavity detaches at the leading edge ($l_0 = 0$), we find that

$$\sigma H(z) - \sigma_0\overline{q}_0(z) = (\sigma - \sigma_0)A(z) \tag{4.19}$$

and therefore

$$H(z) = \frac{\sigma_0}{\sigma}\overline{q}_0(z) + (1 - \frac{\sigma_0}{\sigma})A(z). \tag{4.20}$$

Between the leading edge and the cavity detachment point on the upper surface, the cavity source distribution must match the thickness source distribution, $\overline{q}_w(z)$. From this requirement, we obtain an integral equation whose kernel is a function of $u_c^+ - \frac{1}{2}$:

$$\overline{q}_w(z) - H(z) = \frac{2}{\pi}(1+z^2)\int_0^{t_0}\frac{(u_c^+ - \frac{1}{2})\omega}{(\omega^2 - z^2)(1+\omega^2)}d\omega - \frac{1+z^2}{\pi}\sqrt{\frac{t+z}{z}}\cdot G(z) \tag{4.21}$$

where

$$G(z) \stackrel{\text{def}}{=} -2\cdot\int_0^{t_0}\frac{u_c^+ - \frac{1}{2}}{1+\eta^2}\cdot\frac{\eta}{z-\eta}\left[\frac{1}{z+\eta}\sqrt{\frac{z}{z+t}} - \frac{1}{2\eta}\sqrt{\frac{\eta}{\eta+t}}\right]d\eta. \tag{4.22}$$

By substituting (4.22) in (4.21) and simplifying, we arrive at the final form of the integral equation for $u_c^+ - \frac{1}{2}$:

$$\overline{q}_w(z) - H(z) = \frac{1+z^2}{\pi}\int_0^{t_0}\sqrt{\frac{\eta}{\eta+t}}\frac{(u_c^+ - \frac{1}{2})d\eta}{(1+\eta^2)(\eta-z)}. \tag{4.23}$$

Letting

$$f(\eta) \stackrel{\text{def}}{=} \frac{u_c^+ - \frac{1}{2}}{1+\eta^2} \cdot \sqrt{\frac{\eta}{\eta+t}} \tag{4.24}$$

and writing the integral equation in terms of f,

$$\frac{1}{2\pi} \int_0^{t_0} \frac{f(\eta)d\eta}{\eta - z} = \frac{\overline{q}_w(z) - H(z)}{2} \cdot \frac{1}{1+z^2} \cdot \sqrt{\frac{z}{z+t}} \tag{4.25}$$

we can invert the equation and solve for $f(\eta)$:

$$f(\eta) = -\frac{1}{\pi}\sqrt{\frac{t_0-\eta}{\eta}} \int_0^{t_0} \sqrt{\frac{\omega}{t_0-\omega}}\sqrt{\frac{\omega}{\omega+t}} \cdot \frac{\overline{q}_w(\omega) - H(\omega)}{1+\omega^2} \cdot \frac{d\omega}{\omega - \eta}. \tag{4.26}$$

Finally, substituting equation (4.20) for $H(\omega)$, we obtain

$$u_c^+ - \frac{1}{2} = -\frac{1+\eta^2}{\pi} \cdot \frac{\sqrt{(\eta+t)(t_0-\eta)}}{\eta} \cdot \left[\frac{1}{\sigma} M(z) - \left(1 - \frac{\sigma_0}{\sigma}\right) N(z)\right] \tag{4.27}$$

where

$$M(z) \stackrel{\text{def}}{=} \int_0^{t_0} \sqrt{\frac{\eta}{t_0-\eta}}\sqrt{\frac{\eta}{t+\eta}} \cdot \frac{(q_w - q_0)d\eta}{(1+\eta^2)(\eta - z)} \tag{4.28}$$

and

$$N(z) \stackrel{\text{def}}{=} \int_0^{t_0} \sqrt{\frac{\eta}{t_0-\eta}}\sqrt{\frac{\eta}{t+\eta}} \cdot \frac{A(\eta)d\eta}{(1+\eta^2)(\eta - z)} \tag{4.29}$$

Equation (4.27) is the solution of the integral equation (4.25) which satisfies the condition that $u_c^+ - \frac{1}{2} = 0$ at l_0.

Substituting (4.27) in (4.15), we obtain a more tractable formula for $F(z)$:

$$F(z) = \frac{2}{\pi^2}(1+z^2)\left[\frac{1}{\sigma} M_F(z) - \left(1 - \frac{\sigma_0}{\sigma}\right) N_F(z)\right] \tag{4.30}$$

where

$$M_F(z) \stackrel{\text{def}}{=} \int_0^{t_0} \frac{\sqrt{(\omega+t)(t_0-\omega)}}{\omega^2 - z^2} \cdot M(\omega)d\omega \tag{4.31}$$

and

$$N_F(z) \stackrel{\text{def}}{=} \int_0^{t_0} \frac{\sqrt{(\omega+t)(t_0-\omega)}}{\omega^2 - z^2} \cdot N(\omega)d\omega \tag{4.32}$$

The cavitation number is obtained by applying equation (14.2) of Kinnas' PhD thesis

$$14.2\ of\ [11]: \quad \sigma_0 = \frac{4\sqrt{2}\,r^4}{\pi(r^2+1)} \int_0^t \sqrt{\frac{\eta}{t-\eta}} \cdot \frac{\sqrt{r^2+1}+\eta\sqrt{r^2-1}}{(1+\eta^2)^2} \cdot \frac{d\eta_l}{dx} d\eta$$

and substituting $\frac{d\eta_{l_2}}{dx}$ for $\frac{d\eta_l}{dx}$, where

$$\frac{d\eta_{l_2}}{dx} = \sigma(\Theta^* + F) = \frac{d\eta_l}{dx} + \sigma F$$

which results in:

$$\sigma = \sigma_0 - \sigma \frac{4\sqrt{2}\,r^4}{\pi(r^2+1)} \int_0^t \sqrt{\frac{\eta}{t-\eta}} \cdot \frac{(\sqrt{r^2+1}+\eta\sqrt{r^2-1})}{(1+\eta^2)^2} \cdot F(\eta) d\eta. \tag{4.33}$$

Substituting 4.30 into 4.33, yields

$$\sigma = \sigma_0 - \sigma \left[\frac{1}{\sigma} M_\sigma - \left(1 - \frac{\sigma_0}{\sigma}\right) N_\sigma \right] \tag{4.34}$$

where

$$M_\sigma \stackrel{\text{def}}{=} \frac{8\sqrt{2}\,r^4}{\pi^3(r^2+1)} \int_0^t \sqrt{\frac{\eta}{t-\eta}} \cdot \frac{\sqrt{r^2+1}+\eta\sqrt{r^2-1}}{1+\eta^2} \cdot M_F(\eta) d\eta \tag{4.35}$$

and

$$N_\sigma \stackrel{\text{def}}{=} \frac{8\sqrt{2}r^4}{\pi^3(r^2+1)} \int_0^t \sqrt{\frac{\eta}{t-\eta}} \cdot \frac{\sqrt{r^2+1}+\eta\sqrt{r^2-1}}{1+\eta^2} \cdot N_F(\eta) d\eta. \tag{4.36}$$

Finally, from 4.34 we obtain the new cavitation number

$$\sigma = \sigma_0 - \frac{M_\sigma}{1 - N_\sigma}. \tag{4.37}$$

The new source distribution may be found in a similar way, but it is easier to note that the evaluation of the function $q(z)$ is identical to the case where $l_0 = 0$ except that Θ^* is replaced by Θ_2^*. Θ_2^* is defined in terms of the integrals $M_F(z)$ and $N_F(z)$, which are computed numerically:

$$\Theta_2^*(z) = \Theta^*(z) + \frac{2}{\pi^2}(1+z^2) \left[\frac{1}{\sigma} M_F(z) - \left(1 - \frac{\sigma_0}{\sigma}\right) N_F(z) \right]. \tag{4.38}$$

The vorticity is given by

$$\overline{\gamma}(z) = \overline{\gamma}^*(z) + 2(u_c^+ - \frac{1}{2}) \tag{4.39}$$

where

$$\overline{\gamma}^*(z) = -\frac{1+z^2}{\pi}\sqrt{\frac{t-z}{z}}\int_0^t \sqrt{\frac{\eta}{t-\eta}}\frac{\frac{\eta}{2}-\Theta_2^*(\eta)}{(1+\eta^2)(z-\eta)}d\eta. \tag{4.40}$$

The cavity camber in the wake is still found by equating the slope of the camber to the vorticity downwash, equation (2.23). However, the effect of the upper wetted surface forward of the cavity detachment must be accounted for:

$$\begin{aligned}\frac{1}{\sigma}V_{in}(x) &= -\frac{1}{2\pi}\int_0^1 \frac{\overline{\gamma}^*(\xi)+2(u_c^+-\frac{1}{2})}{\xi-x}d\xi \\ &= -\frac{1}{2\pi}\int_0^1 \frac{\overline{\gamma}^*(\xi)d\xi}{\xi-x} - \frac{1}{\pi}\int_0^{l_0}\frac{u_c^+-\frac{1}{2}}{\xi-x}d\xi\end{aligned} \tag{4.41}$$

which is the same for the case where $l_0 = 0$ with $\Theta_2^*(z)$ in place of $\Theta^*(z)$ and the addition of the second term of equation (4.41).

The solution for $l_0 \neq 0$ depends on the integrals (4.28, 4.29, 4.31, 4.32, 4.35, and 4.36). The integral (4.29) is computed analytically:

$$N(z) = \frac{1}{2\sqrt{2}r^2}\int_0^{t_0}\sqrt{\frac{\eta}{t_0-\eta}}\cdot\frac{a-\eta b}{(1+\eta^2)(\eta-z)}d\eta = \frac{1}{2\sqrt{2}r^2}\left[I_1 - I_2\right] \tag{4.42}$$

where

$$a = \sqrt{r^2-1}; \quad b = \sqrt{r^2+1}; \quad a_0 = \sqrt{r_0^2-1}; \quad b_0 = \sqrt{r_0^2+1}$$

and

$$I_1 \stackrel{\text{def}}{=} a\int_0^{t_0}\sqrt{\frac{\eta}{t_0-\eta}}\cdot\frac{d\eta}{(1+\eta^2)(\eta-z)} = \frac{a\pi}{\sqrt{2}r_o^2(1+z^2)}\cdot(b_0 - za_0) \tag{4.43}$$

and

$$I_2 \stackrel{\text{def}}{=} b\int_0^{t_0}\sqrt{\frac{\eta}{t_0-\eta}}\cdot\frac{\eta d\eta}{(1+\eta^2)(\eta-z)} = \frac{b\pi}{\sqrt{2}r_0^2(1+z^2)}(a_0 + zb_0). \tag{4.44}$$

Equations (A.20) and (A.26) of Kinnas' PhD thesis have been applied in computing (4.43) and (4.44). Finally, we have

$$N(z) = \frac{\pi}{4r^2r_0^2}\cdot\frac{1}{1+z^2}\cdot\left[(ab_0 - ba_0) - z(aa_0 + bb_0)\right]. \tag{4.45}$$

The remaining integrals are computed numerically by factoring out the singularity and transforming to an angular coordinate. An example is the computation of (4.28):

$$M(z) = \int_0^{t_0} \sqrt{\frac{\eta}{t_0 - \eta}} \cdot \frac{f(\eta)d\eta}{\eta - z} \tag{4.46}$$

where

$$f(\eta) = \sqrt{\frac{\eta}{\eta + t}} \cdot \frac{q_w - q_0}{1 + \eta^2}. \tag{4.47}$$

Subtracting out the singularity

$$M(z) = \int_0^{t_0} \sqrt{\frac{\eta}{t_0 - \eta}} \cdot \frac{f(\eta) - f(z)}{\eta - z} d\eta + f(z) \cdot \int_0^{t_0} \sqrt{\frac{\eta}{t_0 - \eta}} \cdot \frac{d\eta}{\eta - z}. \tag{4.48}$$

The second integral of (4.48) is computed analytically via equation (A.4) of [11]:

$$\int_0^{t_0} \sqrt{\frac{\eta}{t_0 - \eta}} \cdot \frac{d\eta}{\eta - z} = \begin{cases} \pi \, \mathrm{f(z)} & 0 \le z \le t_0 \\ (\pi - \pi\sqrt{\frac{z}{z - t_0}}) \, \mathrm{f(z)} & z > t_0 \end{cases}$$

With the transformation

$$z = t sin^2 \frac{\phi}{2}; \quad \eta = t_0 sin^2 \frac{\theta}{2}; \quad 0 < \theta, \phi < \pi \tag{4.49}$$

the first integral of (4.46) becomes

$$M(\phi) = \int_0^{\pi} \frac{f(\theta) - f(\phi)}{t_0 sin^2 \frac{\theta}{2} - t sin^2 \frac{\phi}{2}} \cdot t_0 sin^2 \frac{\theta}{2} d\theta \tag{4.50}$$

and this integral is computed via Simpson's rule.

The remaining integrals are computed in a similar way. The result is a system of nested singular integrals for which special care is taken when the integrals are computed a point which coincides, or nearly coincides, with a step of the Simpson's integration (i. e. , when z is close to η in (4.48)). For a system of nested singular integrals which are all computed with roughly the same number of Simpson intervals, this can happen quite often. The solution to this problem was to use a first order difference approximation of the integrand whenever $abs(z - \eta) < t sin^2 \frac{\epsilon}{2}$ as, for example, for (4.50):

$$M(\phi) \approx \int_0^{\pi} \frac{f(\phi + \epsilon) - f(\phi - \epsilon)}{t sin^2 \frac{\phi + \epsilon}{2} - t sin^2 \frac{\phi - \epsilon}{2}} \cdot t_0 sin^2 \frac{\theta}{2} d\theta. \tag{4.51}$$

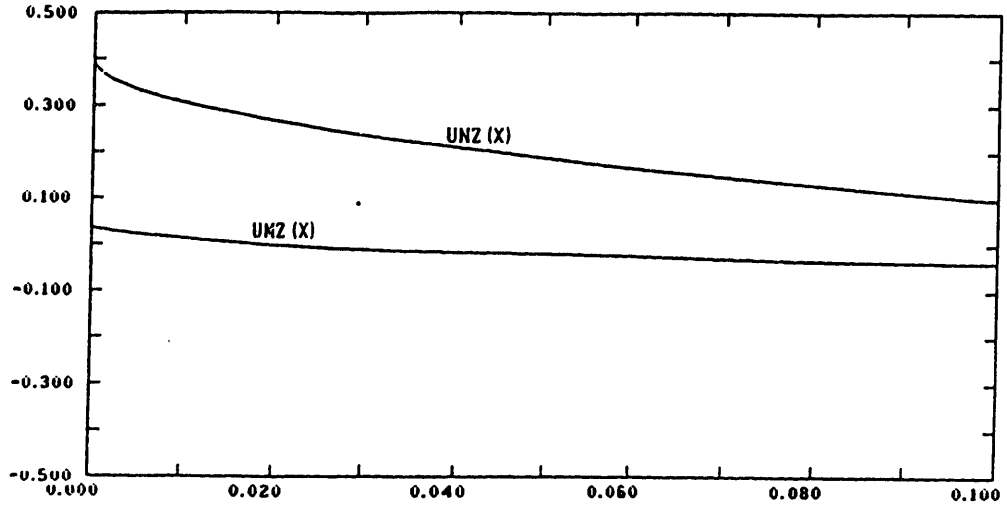

Figure 4.7: The functions $M(z)$ and $N(z)$ for $l_0 = .1$

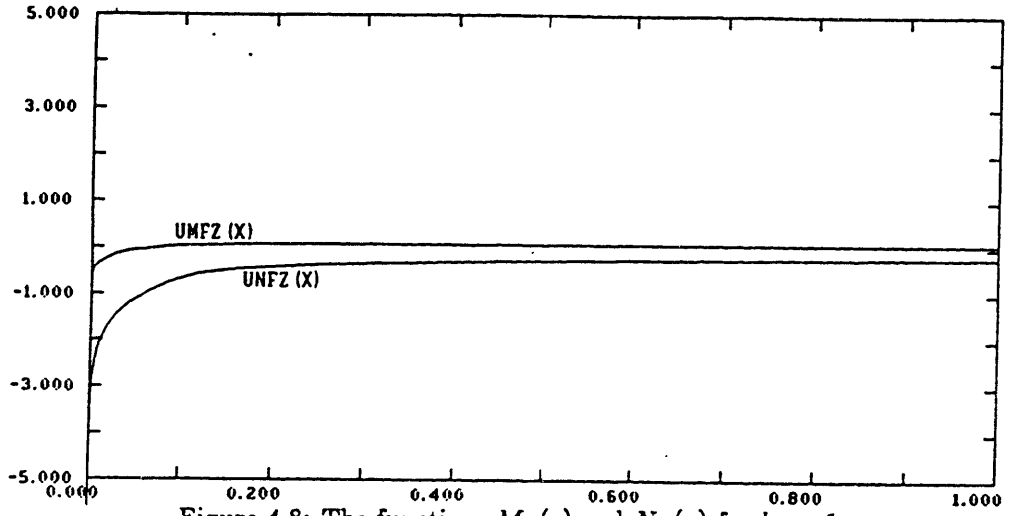

Figure 4.8: The functions $M_F(z)$ and $N_F(z)$ for $l_0 = .1$

The functions $M(z)$, $N(z)$, $M_F(z)$, and $N_F(z)$ are shown in Figures 4.7 and 4.8, where they have been plotted in the x coordinate for the case $l_0 = .10$. Note that M(z) and N(z) are shown for the domain $0 < x < l_0$, corresponding to the z-domain $0 < z < t_0$. Although they are strictly defined only in this region, they are evaluated throughout the region $0 < x < 1$ (or $0 < z < t$) due to the factoring of singularities in the computation of M_σ and N_σ. It can be shown, however, that M(z) and N(z) can be considered to be constant for $l_0 < x < 1$ ($t_0 < z < t$) and equal to their values at the point $x = l_0$ ($z = t_0$).

4.3.2 Results

The analysis of the preceding section has been implemented in the analytic solution. Figure 4.9 shows typical results for an arbitrary foil which may cavitate under conditions of midchord detachment. The plot of cavity source distribution superimposed on the foil thickness source distribution is an indication that the theory and computations produce the desired results. However, a condition has not yet been derived which, when satisfied, finds the correct point of detachment. Franc and Michel [5] have suggested that the detachment point is determined by the condition that the cavity starts just downstream of the point of laminar separation. This condition has not yet been implemented, and the detachment point remains an input to the analysis. However, this type of criterion concedes that the fluid forward of the detachment point may be in tension, which is evident in the ideal flow calculations of the pressure distribution (Figures 4.10 - 4.17). In the Figures, the foil is at such a small angle of attack that the $l_0 = 0$ solution cuts the foil and is clearly wrong. However, as the cavity detachment point is moved aft to the point where the cavity no longer cuts the foil, the pressure on the wetted surface forward of the detachment remains less than the pressure on the cavity (thereby violating the prime directive of cavity detachment points).

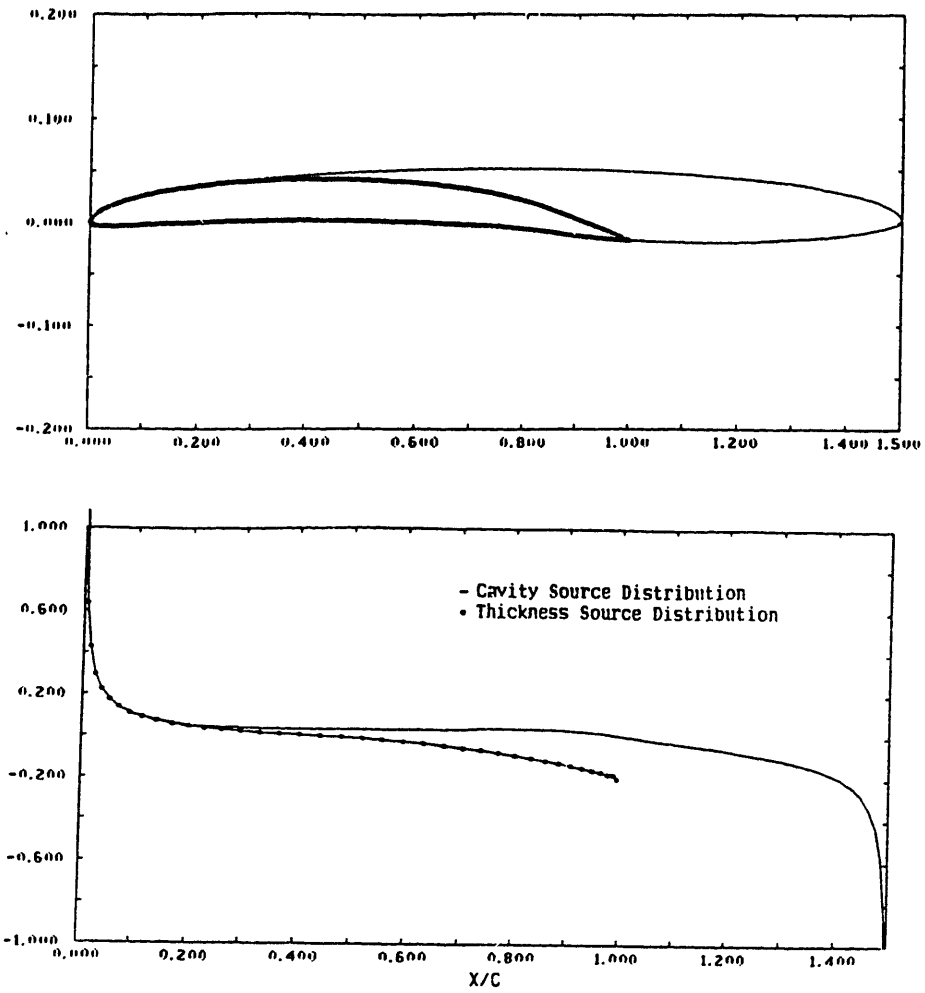

Figure 4.9: VLR thickness profile with NACA a=.8 meanline supercavitating with midchord detachment $l_0 = .20$. Below is thickness source distribution superimposed on cavity source distribution.

For a supercavitating thick symmetric foil at zero angle of attack, the cavity must be symmetric and, therefore, the chordwise coordinate of the cavity detachment points on the upper and lower surfaces must match. Although we have a criterion for finding the detachment point on the lower side of the foil, X_s, it depends on the midchord detachment point, l_0, and this is unknown. However, by coupling the two problems, it is possible to input both parameters with a starting guess influenced by our experience with finding the correct X_s. The results of this experiment are shown in Figure 4.18. The pressure distribution again shows that the fluid is in tension forward of the detachment point. These results indicate that the correct detachment point on the suction side depends on viscous effects; namely, the point of detachment must be preceded by laminar separation in the boundary layer.

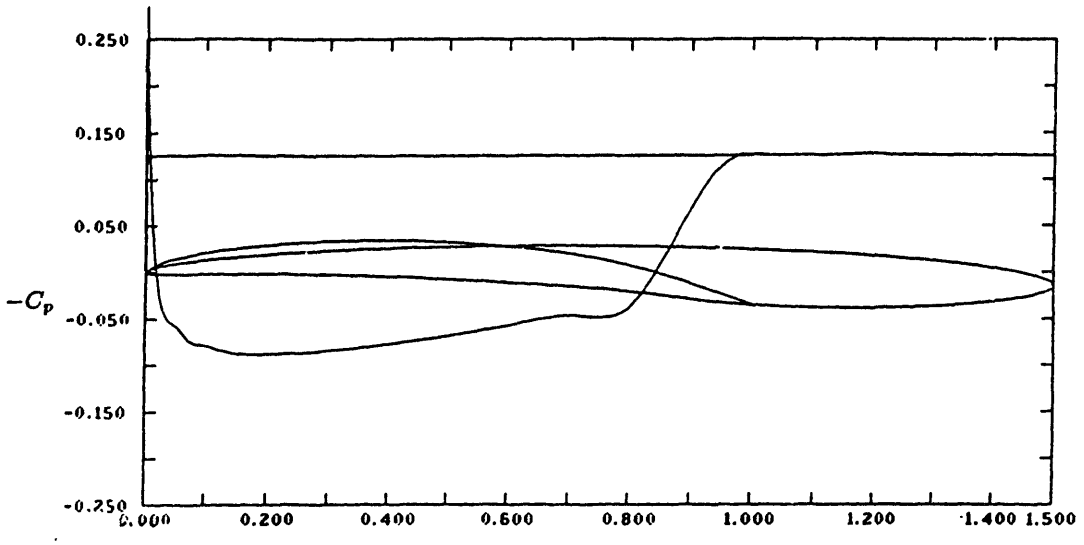

Figure 4.10: Supercavitating foil and superimposed pressure distribution with $l_0 = 0$

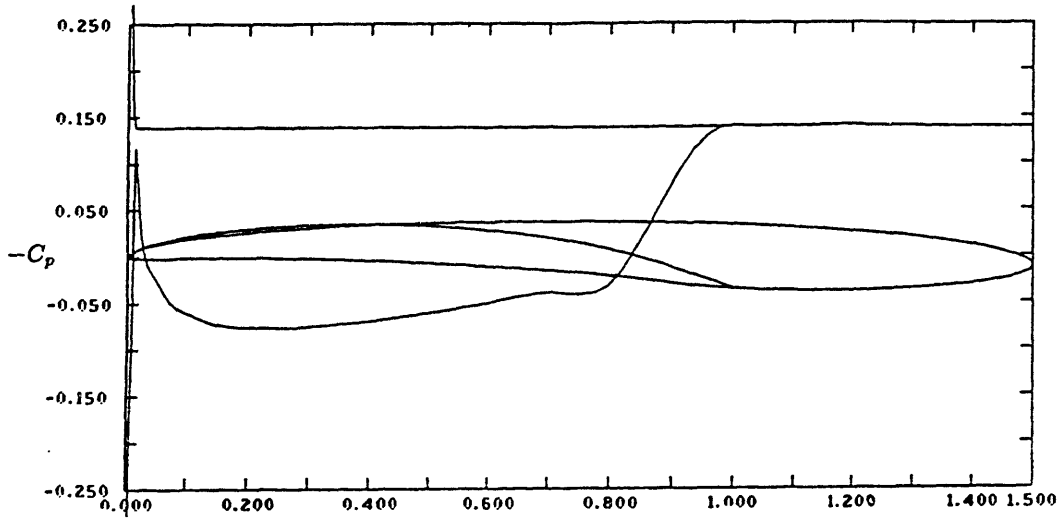

Figure 4.11: Supercavitating foil and superimposed pressure distribution with $l_0 = .01$

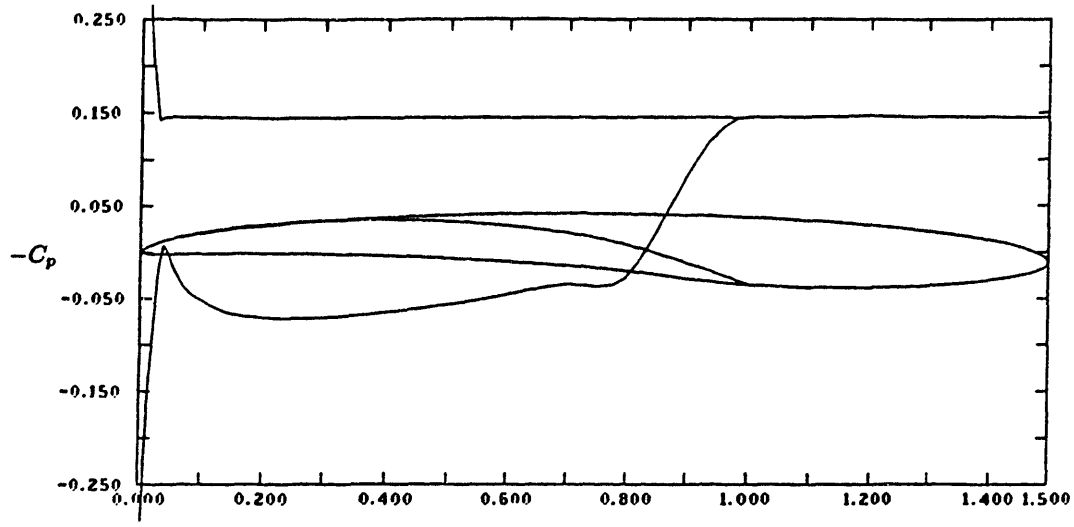

Figure 4.12: Supercavitating foil and superimposed pressure distribution with $l_0 = .03$

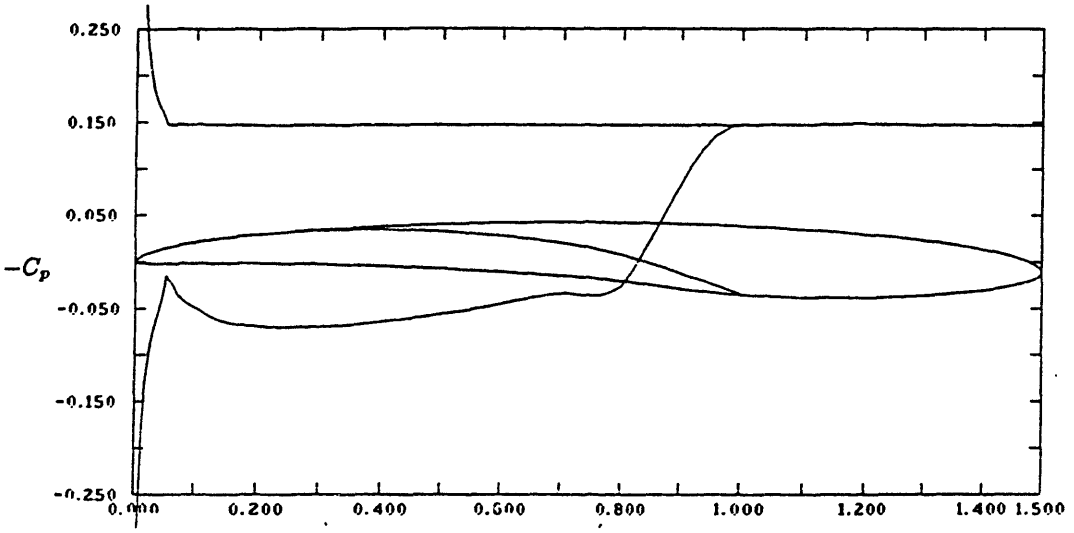

Figure 4.13: Supercavitating foil and superimposed pressure distribution with $l_0 = .05$

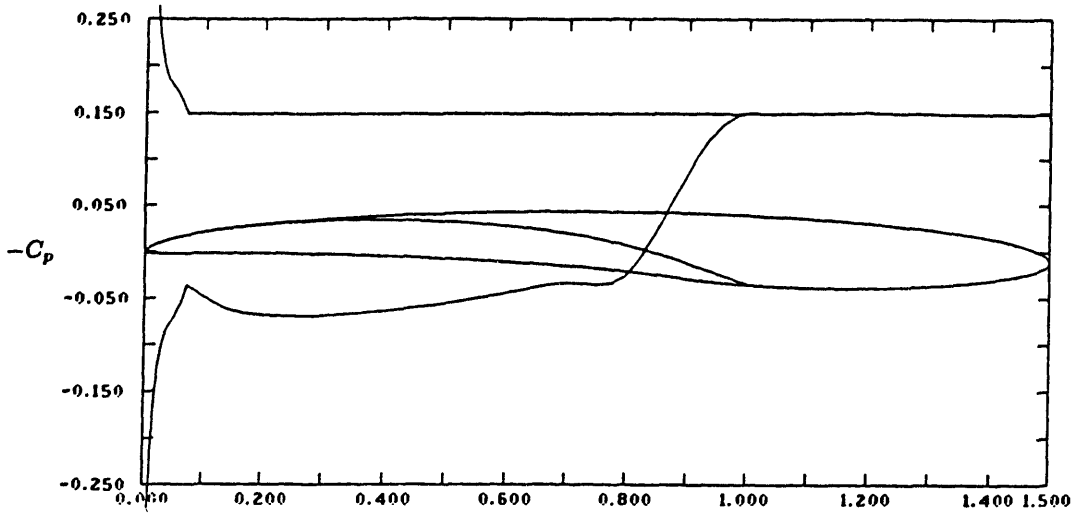

Figure 4.14: Supercavitating foil and superimposed pressure distribution with $l_0 = .07$

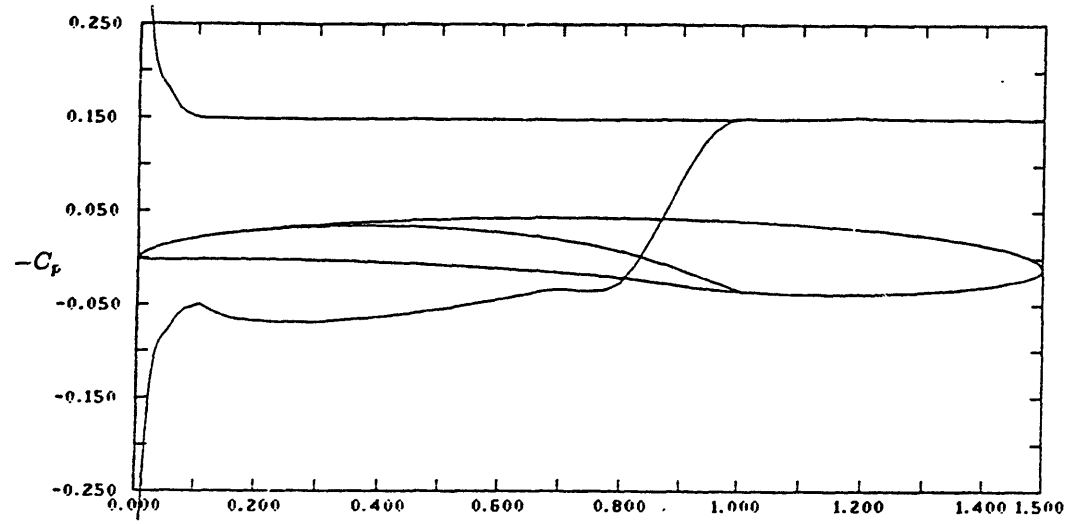

Figure 4.15: Supercavitating foil and superimposed pressure distribution with $l_0 = .10$

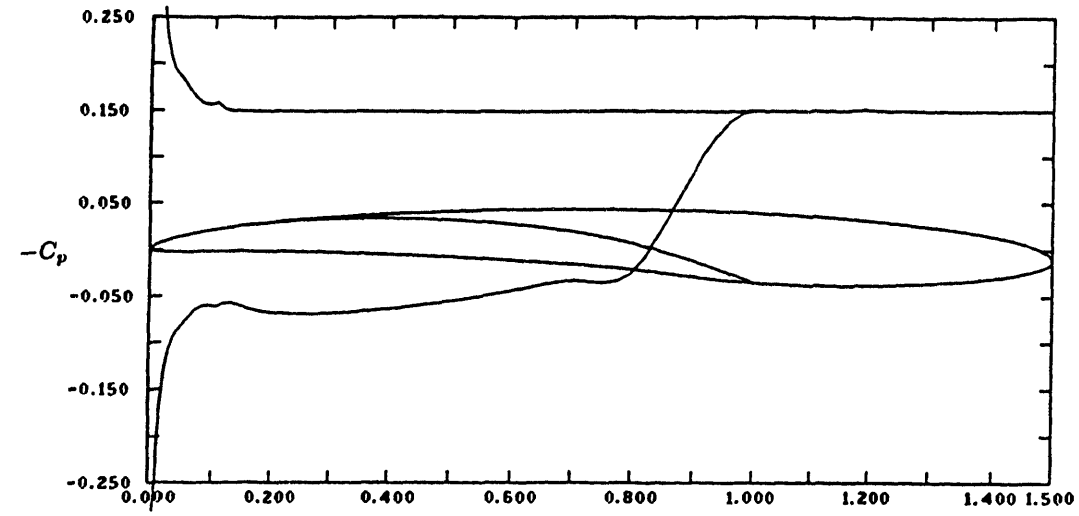

Figure 4.16: Supercavitating foil and superimposed pressure distribution with $l_0 = .15$

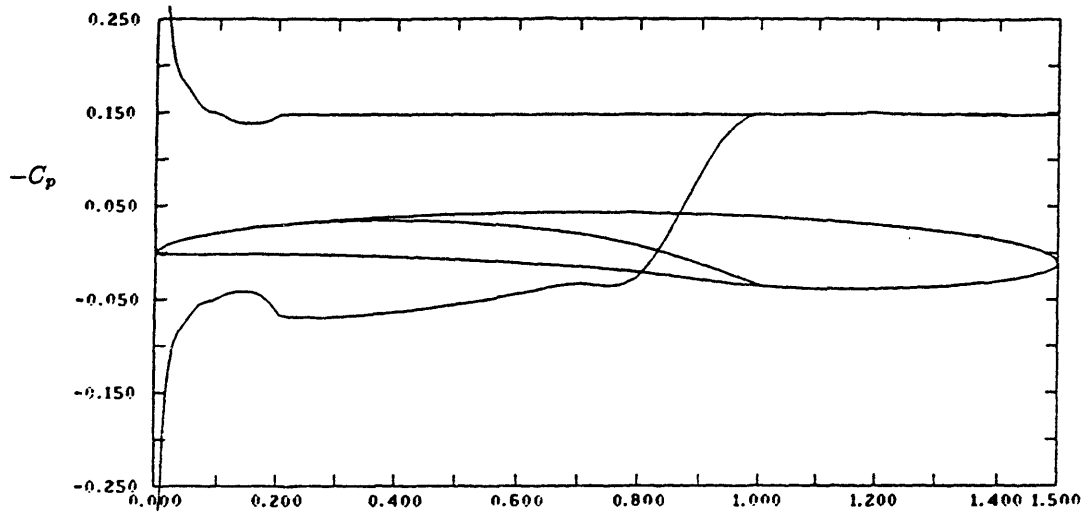

Figure 4.17: Supercavitating foil and superimposed pressure distribution with $l_0 = .20$

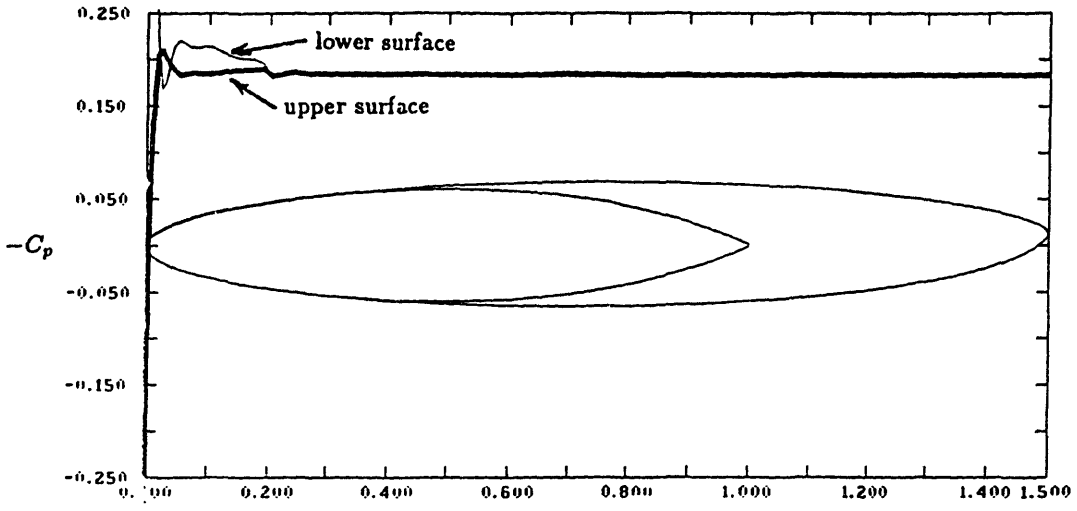

Figure 4.18: Supercavitating thick symmetric foil at zero angle of attack showing midchord detachment and face cavitation

Chapter 5

Conclusions and Recommendations

5.1 Conclusions

A robust and flexible code has been developed for computing the flow around partially and supercavitating hydrofoils by a numerical method and by the semi-analytic method of Kinnas. Convergence tests have shown that the method of discrete singularities is accurate, as well as computationally efficient.

The open cavity model was implemented for partial cavitation. The results compare well with analytic results, providing δ is small.

An experiment was performed to measure the thickness of the cavity wake for a partially cavitating VLR thickness form with NACA a=.8 meanline. The wake thickness was found to be small ($O(10^{-3})$) and constant along the foil after the cavity trailing edge. δ increased in proportion to the length of the cavity.

The measured cavitation number was compared to the numerically obtained cavitation number for four cavity lengths, showing excellent agreement. To make this comparison, the tunnel wall effect was included in the numerical model via the method of images; the effect of the boundary layer was incorporated by use of an effective angle of attack, as suggested by Pinkerton [15]. In addition, the open cavity model was used, as well as the non-linear leading edge corrections.

Finally, the problems of face cavitation and midchord detachment have been solved. For face cavitation, a criterion has been developed for determining the correct point of detachment which depends only on the foil geometry, the cavity length, and the point of midchord detach-

ment on the suction side. A similar criterion for midchord detachment is under consideration; it has been recognized, however, that the criterion may rely on knowing the behavior of the viscous boundary layer.

5.2 Recommendations

The following tasks remain at the conclusion of this research:

1. The open cavity model should be implemented in PUF-3, the propeller analysis code.
2. The analysis for face cavitation should immediately be included in PUF-3, since it requires few changes to the code.
3. A reliable criterion should be developed to determine the midchord detachment point.
4. The analysis for midchord detachment should be applied to the method of discrete singularities in two dimensions, and later to the vortex lattice method in three dimensions.
5. A valuable one-day project would be to measure the pressure distribution at many more points on the foil used in the experiment (top *and* bottom) and superimpose the results on Figure 3.8. This would be a further check of the effective angle of attack and could confirm the results of Pinkerton.

Bibliography

[1] R. Babeau and R. Latorre. Technique for predicting the influence of walls on the boundary layer on two dimensional foils. 1987. Presented and distributed at the International Symposium on Cavitation Research Facilities and Techniques.

[2] G. Birkhoff and E.H. Zarantonello. *Jets, Wakes and Cavities.* Academic Press Inc., New York, 1957.

[3] C.N. Corrado. *Investigations of Numerical Schemes for the Evaluation of the Cavitating Flow Around Hydrofoils.* Technical Report 86-6, MIT, 1986.

[4] A.G. Fabula. Thin-airfoil theory applied to hydrofoils with a single finite cavity and arbitrary free streamline detachment. *Journal of Fluid Mechanics*, vol 12:pp 227–240, 1962.

[5] J.P. Franc and J.M. Michel. Attached cavitation and the boundary layer: experimental investigation and numerical treatment. *Journal of Fluid Mechanics*, vol. 154:pp 63–90, 1985.

[6] D.W. Golden. *A Numerical Method for Two Dimensional Cavitating Lifting Flows.* Technical Report 81512-1, MIT, 1975.

[7] R.M. James. On the remarkable accuracy of the vortex lattice method. *Computer Methods in Applied Mechanics and Engineering*, vol. 2, 1972.

[8] J.E. Kerwin, S.A. Kinnas, M.B. Wilson, and McHugh J. Experimental and analytical techniques for the study of unsteady propeller sheet cavitation. In *Proceedings of the Sixteenth Symposium on Naval Hydrodynamics*, Berkeley, California, July 1986.

[9] S.A. Kinnas. *Cavity Shape Characteristics for Partially Cavitating Hydrofoils.* Technical Report 85-1, MIT, Department of Ocean Engineering, February 1985.

[10] S.A. Kinnas. *Cavity Shape Characteristics for Supercavitating Hydrofoils.* Technical Report 84-13, MIT, Department of Ocean Engineering, October 1984.

[11] S.A. Kinnas. *Non-linear Corrections to the Linear Theory for the Prediction of the Cavitating Flow Around Hydrofoils.* Technical Report 85-10, MIT, Department of Ocean Engineering, June 1985.

[12] C.E. Lan. A quasi vortex-lattice method in thin wing theory. *Journal of Aircraft*, vol. 11(no. 9), 1974.

[13] C.S. Lee. *Prediction of Steady and Unsteady Performance of Marine Propellers With and Without Cavitation by Numerical Lifting Surface Theory.* Technical Report, MIT, 1979.

[14] J.N. Newman. *Marine Hydrodynamics.* The MIT Press, Cambridge, Massachusetts, 1977.

[15] R.M. Pinkerton. *Calculated and Measured Pressure Distributions over the Midspan of the N.A.C.A. 4412 Airfoil.* Technical Report 563, N.A.C.A., 1936.

[16] S.A.Kinnas. Leading edge corrections to the linear theory of partially cavitating hydrofoils. 1988. Submitted for Publication to the Journal of Fluid Mechanics.

[17] S.A.Kinnas and N.E. Fine. Theoretical prediction of midchord and face unsteady propeller sheet cavitation. 1989. To be considered for publication at the Fifth International Conference on Numerical Ship Hydrodynamics.

[18] M.P. Tulin. *Steady Two-Dimensional Cavity Flows About Slender Bodies.* Technical Report 834, DTMB, May 1953.

[19] M.P. Tulin. Supercavitating flows - small perturbation theory. *Journal of Ship Research*, vol 7(No. 3):pp. 16–37, 1964.

[20] J.S. Uhlman. The surface singularity method applied to partially cavitating hydrofoils. *Journal of Ship Research*, vol 31(No. 2):pp. 107–124, June 1987.

[21] R. J. Van Houten, J. E. Kerwin, and J. S. Uhlman. Numerical solutions of lifting surface sheet cavitation - a review of research at m.i.t. In *20th American Towing Tank Conference*, Stevens Institute of Technology, 1983.